Science Advances
AAAS

Supplementary Materials for

Modular architecture facilitates noise-driven control of synchrony in neuronal networks

Hideaki Yamamoto *et al.*

Corresponding author: Hideaki Yamamoto, hideaki.yamamoto.e3@tohoku.ac.jp;
Jordi Soriano, jordi.soriano@ub.edu

Sci. Adv. **9**, eade1755 (2023)
DOI: 10.1126/sciadv.ade1755

The PDF file includes:

Other Supplementary Material for this manuscript includes the following:

1. SUPPLEMENTARY VIDEOS AND EXTENDED EXPERIMENTAL RESULTS

A. Supplementary Videos

Videos encompass both experimental recordings and numerical simulations of networks of spiking neurons. The videos corresponding to experimental recordings are played at 20× speed. The left-hand side of the videos shows the recording, while the right-hand side shows the raster plot derived from its analysis. The original image sequences were obtained in greyscale format and here are presented as a blue–red–yellow color scheme to enhance the visualization of activity. The brighter the color, the stronger the activity of the neurons. For modular networks, each of the 4 modules is highlighted with a faint colored outline, where the color matches the grouping of spikes and module rates on the right.

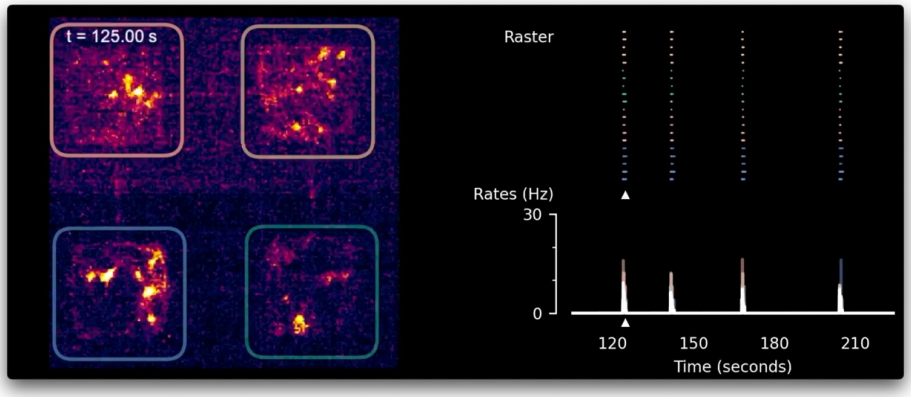

Video 1. Single–bond network during spontaneous activity.
These recordings and their raster plots are the same ones shown in Figs. 1D–G of the main manuscript.
Video 2. Same network as in Video 1 but under optogenetic stimulation.

Video 3. Single–bond network during spontaneous activity before chemical stimulation with potassium.
The raster plots correspond to the data shown in Figs. 1H–I of the main manuscript.
Video 4. Same as network as Video 3 but after chemical stimulation with high potassium.

Video 5. Single–bond network during spontaneous activity while exposed to bicuculline.
Video 6. Single–bond network exposed to bicuculline under optogenetic stimulation.

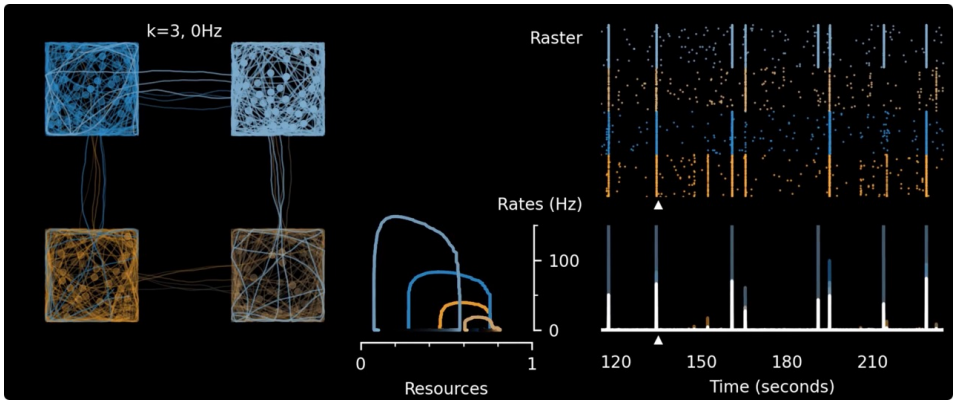

Video 7. Simulations, model of spiking neurons with modules connected by $k = 3$ axons, with neurons receiving only baseline noise.
Video 8. Same network and random number seed as Video 7 but neurons in the lower two modules receive 20 Hz additional noise beyond baseline.

B. Comparison of Different Optogenetic Stimulation Paradigms

In the following, we describe two control experiments to investigate i) the role of how many modules are targeted (partial vs global stimulation) and ii) the impact of asynchronous vs synchronous stimulation (Fig. S1). We focus on modular, single-bond topologies. Note that for these new control experiments, substrates differ from the main manuscript: Cultured cortical neurons were patterned using *microfluidic devices* [83], which we found to provide more reproducible results. The four modules again consist of 200 µm × 200 µm squares that are connected by microchannels of three different sizes to adjust the degree of modularity (S: 4 µm width × 2 µm height, M: 7 × 2 µm, L: 7 × 4 µm). All experiments were conducted at 10–11 DIV, as in the other experiments. For each channel size, we considered three stimulation protocols:

- `stim 2` is the protocol described in the main manuscript. The lower two modules are targeted by asynchronous optogenetic stimulation, where ten individual neurons are preselected candidates to be targeted (during each 400 ms time bin, every candidate has a probability $p = 0.4$ to be stimulated).
- `stim 4` is similar to the protocol of the main manuscript, but two to three candidates are selected from each of the four modules (ten in total). Note that, due to an experimental constraint, the area from which neurons can be selected is limited, so that candidates do not cover the whole culture.
- `stim 1` is a synchronous stimulation protocol, where the entire area of one of the four modules was targeted with a square light pulse of 400 ms. The pulses were delivered at a mean interval of 10 s with a standard deviation of 2 s.

Partial stimulation: We first confirmed the reproducibility of the experiments reported in the main manuscript by applying protocol `stim 2`. As shown in the example raster plots (Fig. S1A), collective activity events present in the spontaneous activity (`pre`) were disrupted during stimulation, which decreased the overall neuron correlation and event size (Fig. S1B) and recovered during `post` (not shown). The decrease in correlation was also observed when the optogenetic stimulation was delivered locally, to one of the four modules (`stim 1`, Fig. S1B). However, note that the typical response of the cultures to the `stim 1` differed to `stim 2`: The synchronous stimulation reliably triggered bursting activity, causing an event that started in the targeted module and probabilistically propagated to neighbouring modules, potentially spanning the whole system. This observation is in line with the gating mechanism that we abstractly model in the mesoscopic description (Section 3, below). The asynchronous stimulation, on the other hand, did not trigger events deterministically at pre-defined times. This can be seen as a confirmation of our proposed resource mechanism. Reconsidering the recharge dynamics (main Fig. 4A–C), the perturbing effect of the `stim 1` protocol should vanish if the delivery of the pulse is timed to match the intrinsic, natural timing of events each culture has. In this case, the duration of charge-discharge cycles would not be altered, merely the onset-times of events. On the other hand, if pulses are delivered at a higher frequency, resources would be depleted more often. To confirm this intuition, we color-coded the lines representing each culture according to its (natural) IEI during the `pre` condition (Fig. S1). For `stim 1`, and channel size M in particular, this intuition seems confirmed: Those realizations where the IEI was already short before the stimulation at 1/10 s (yellow and red) tend to show smaller changes.

Global stimulation: As presented in Fig. 1 of the main manuscript, a global increase in neuronal excitablility induced by chemical stimulation did not break synchrony in modular networks. To address the question whether global but asynchronous stimulation does break synchrony, we applied the protocol `stim 4`. Overall, the results for this protocol show the same trends as for `stim 2`, with decreased event sizes and neuron correlations, and a strong dependence on the topology.

Channel size: The most consistent trend in the results of these new control experiments is the dependence on channel size. In particular, for large channels (L), where presumably connections between modules are strong and modularity low, the effect size of all stimulation protocols tends to be smallest. This supports our main conclusion, that the modularity of the topology is the key ingredient to facilitate the desynchronizing effect of stimulation.

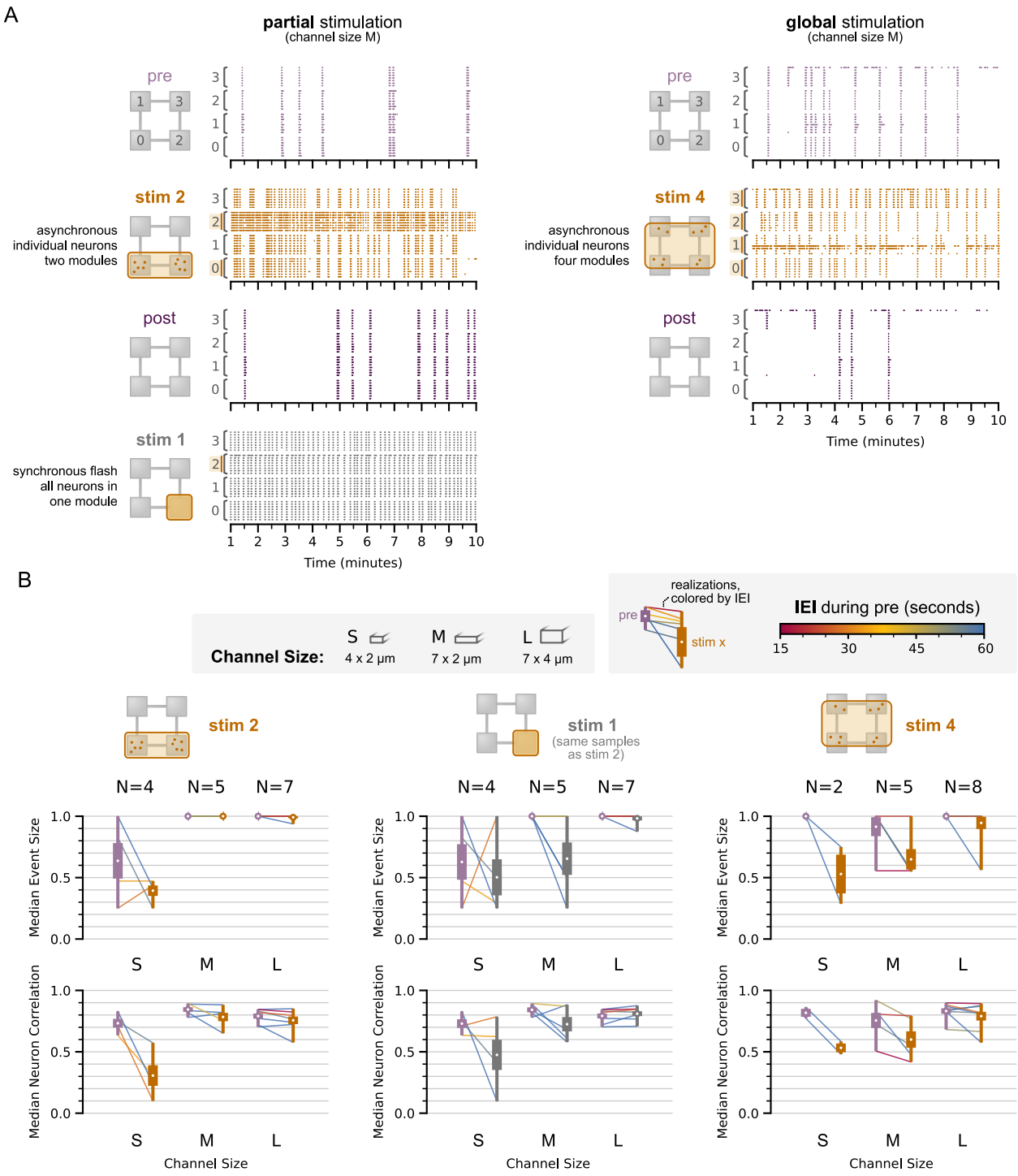

Figure S1. **Comparison of different optogenetic stimulation paradigms. A:** Raster plots. As controls of the asynchronous stimulation in two modules `stim 2` (main manuscript), we considered two other stimulation paradigms. In `stim 1`, a single module was targeted with a flash covering the whole module every ∼10 s. Thus, the stimulation was *synchronous* (to all neurons of this module) and *partial*, as only a subset of the modules was targeted. Notably, flashes reliably cause events that span at least the targeted module. In `stim 4`, individual neurons from all modules were targeted *asynchronously*, similar to `stim 2` but extending the stimulation region to the full system (*global*). However, note a constraint of the experimental setup that limited the location of neurons that could be targeted to parts of each module. **B:** For these stimulation paradigms, we compare the `pre` condition with the respective `stim` condition, for three different channel sizes, S, M, and L. Note that the samples for partial stimulation (`stim 2` and `stim 1`) are correlated, as they were recorded in sequence, from the same cultures. For each realization, the line connecting `pre` and `stim` is color-coded by the mean inter-event-interval (IEI, measured during the `pre` condition). This serves as a proxy for the strength of the perturbation caused by `stim 1`: In this paradigm, the impact of stimulation on the recharge dynamics is presumably small when the frequency of the flash (every ∼10 s) is close to the intrinsic IEI (red for 15 s, blue for 60 s). Because asynchronous stimulation (`stim 2`, `stim 4`) targets individual neurons, and does not trigger events that span a whole module, this dependence seems less pronounced. Independent of the stimulation protocol, note the dependence on channel size (as an indicator for modularity): With increasing channel size, the effect from all considered forms of stimulation decreases.

C. Effect of the Blockade of Inhibition on Dynamics

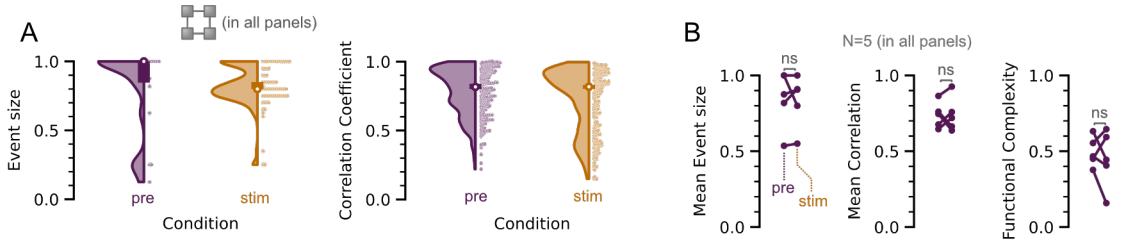

Figure S2. **The desynchronizing effect of optogenetic stimulation relies on GABAergic balancing**. Data collected on 1-b modular networks ($N = 5$ trials) in the presence of 20 µM bicuculline, a $GABA_A$ receptor antagonist. The data for this assay was collected using 1-b modular networks grown in both microcontact printed substrates and microfluidic devices (Ref. [83], different samples from those analyzed in the previous section). **A:** Aggregated distributions of network-wide events (left) and pairwise correlation coefficients (right). **B:** Trial-to-trial estimates of the mean event size, mean correlation, and functional complexity. ns, no significance (two-sided, paired-sample t-test). We note that administration of bicuculline at 20 µM may seize or substantially decrease the rate of spontaneous activity in small-scale neuronal networks, such as those used in the present work, at 10–11 DIV. In such a case, similar effects could be observed at a concentration of ∼5 µM.

D. Statistics across Experimental Repetitions

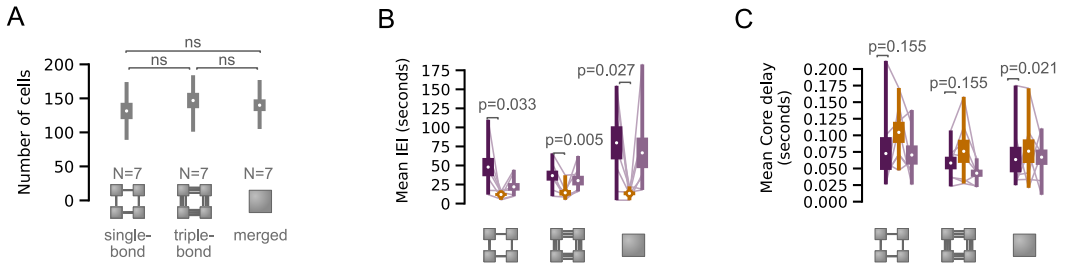

Figure S3. **Trial-level estimates,** related to main Fig. 2. **A:** Mean number of cells per network. The differences between the means of the three topologies are statistically not significant. Two-sided, unpaired t-test. **B, C:** Every faint line corresponds to the estimate of a quantity within one trial and its change across conditions (pre, stim and post). Error bars (thick vertical lines) are obtained from bootstrapping the within-trial estimates (500 samples). The white dot denotes the mean of the bootstrap samples, and the extended thin vertical line indicates the maximal and minimal value observed in a trial. The indicated statistical significance (pre to stim) is calculated from two-sided, paired-sample t-tests. For p-values of all combinations, see Table S1.

Layout	**Comparison**	Rate	Event size	Neuron correlation	Functional complexity	IEI	Core delay
1b ($N = 7$ trials)	pre-stim	0.8411	0.0067	0.0084	0.0524	0.0338	0.1557
	stim-post	0.6910	0.0130	0.0071	0.0037	0.1033	0.0719
	pre-post	0.9685	0.1749	0.9631	0.5391	0.1219	0.8875
3b ($N = 7$ trials)	pre-stim	0.2072	0.0513	0.0335	0.0384	0.0057	0.1556
	stim-post	0.2957	0.0617	0.0103	0.0170	0.0428	0.0647
	pre-post	0.3505	0.6590	0.9678	0.0666	0.4373	0.0898
merged ($N = 7$ trials)	pre-stim	0.0284	0.0463	0.0195	0.0469	0.0278	0.5641
	stim-post	0.1773	0.0542	0.0181	0.0560	0.0678	0.6848
	pre-post	0.6078	0.4167	0.3847	0.9992	0.7199	0.8951

Table S1. Overview of p-values for Main Fig. 2 and Suppl. Fig. S3. Two-sided, paired-sample t-test.

2. DETAILS OF THE MICROSCOPIC MODEL OF SPIKING NEURONS

A. Topology

To create the 2D topology, we model axonal growth as proposed by Orlandi et al. [18] (cf. Table S3). Neurons are spread out uniformly over a 2D surface where somas are modeled as hard, non-overlapping discs with radius $r_\mathrm{s} = 7.5\,\mu\mathrm{m}$ from which axons grow on a semi flexible path with mean length $l_\mathrm{a} \approx 1000\,\mu\mathrm{m}$. The path is constructed from several concatenated axonal segments of unit length $\delta_\mathrm{a} = 10\,\mu\mathrm{m}$. The variance of the mean bending angle $\sigma(\theta)$ along neighboring segments determines the overall stiffness. If an axon intersects the dendritic tree of another neuron (modeled as soft disks with mean radius $r_\mathrm{d} \approx 150\,\mu\mathrm{m}$), then each overlapping segment has probability α to establish the connection. (Note, this is a different convention than Ref. [18], where the probability to form the connection is independent of the number of intersecting segments.) Because dynamics are heavily dependent on the in-degree, we adjust α so that $k_\mathrm{in} \approx 30$ incoming connections per neuron [82] for all topologies, independent of their modularity. Once the connections are set (as a binary matrix), additional details of the topology can be discarded. The types of neurons (inhibitory GABAergic or excitatory AMPA-glutamatergic) are not distinguished topologically.

In order to create the modular topology, soma, axon segments, and dendritic trees are only placed on the substrate, which consists either of one $400 \times 400\ \mu\mathrm{m}^2$ rectangle (merged) or four $200 \times 200\ \mu\mathrm{m}^2$ rectangles (modular). To avoid axons growing out of the substrate, larger bending angles (with increased variance $\sigma(\theta') = 5\sigma(\theta)$) are allowed near the domain walls, which effectively deflect the axons back into the module (main Fig. 3A). To connect neighboring modules with a given number of axons, every module acts once as a "source module". Then, for every adjacent neighboring module, k neurons are selected and forced to first grow their axons towards the center of the target module (neglecting the substrate) before the growth continues randomly within the target, again confined to the substrate. The in-degree distributions for the different topologies are summarized in Fig. S5.

We found this controlled approach to produce more consistent topologies than an algorithm where we would add a given number of bridges as an actual part of the substrate (as in the experiments) and axons had to grow through the bridges by chance. For the latter case, it frequently occurred that modules were only connected in one direction or not connected at all. As the topological structure is the backbone of the observed dynamics, a much larger number of repetitions would have been needed to find reliable ensemble estimates of observables.

B. Modularity

In the following, we show analytically how the modularity index Q depends on the number of axons crossing between modules ($\mathbf{k}$) and the in-degree per neuron (k_{in})[1]. The straightforward mathematical way of measuring how well a partition splits the graph into modules is computing the *modularity*—the fraction of the edges that fall within the given groups minus the expected fraction if edges were distributed at random [84]. While using this measure to find community division is criticized [85], in our case, communities are already defined (as modules) per the experimental or theoretical construction, and we evaluate the modularity for this partitioning.

Modularity is formally defined as:

$$Q = \frac{1}{2m} \sum_{ij} \left(A_{ij} - \gamma \frac{k_i k_j}{2m} \right) \delta(c_i, c_j), \tag{1}$$

where m is the total number of edges, A_{ij} is the adjacency matrix of the graph, k_i is the degree of node i, γ is the resolution parameter that we take, $\gamma = 1$, and $\delta(c_i, c_j)$ is 1 if nodes i and j belong to the same community and 0 otherwise. The summation is performed over all pairs of nodes in the network. The simplified formula for Q reads:

$$Q = \sum_{c=1}^{n} \left[\frac{L_c}{m} - \gamma \left(\frac{k_c}{m} \right)^2 \right], \tag{2}$$

where summation is performed over all modules c, L_c is number of links within a module, and k_c is the sum of the degrees of all nodes of the module.

When growing the networks with axons crossing over between modules, we control the mean in-degree per neuron. To do so, we need to adjust the expected density of connections per unit length α. Let us compute the number of

[1] Note that the number of axons that cross to neighbouring modules is denoted by k in the rest of the material. In this section, we denote it as $\mathbf{k}$ to differentiate from other degree-related variables.

connections, assuming N neurons in the module and $\mathbf{k}$ neurons that would form a cross-module axon per neighbour. In this case, the total number of connections between neurons of the same module (L_c) is a sum of connections due to axons not crossing modules plus connections due to the parts of crossing axons that are still within the same module. With our model parameters (200 µm module size / separation and $l_a \approx 1000$ µm axon length) a crossing axon spends ~ 100 µm in the source module, ~ 200 µm between modules, and ~ 700 µm in the target module. Thus, the number of connections within the same module L_c is given by

$$L_c = (N - 2\mathbf{k})\alpha \cdot l_a + 0.1 \cdot 2\mathbf{k} \cdot \alpha \cdot l_a = (N - 1.8\mathbf{k})\alpha \cdot l_a. \tag{3}$$

The number of connections coming from the two other neighbouring modules is proportional to the axon parts they have within the target module, $0.7l_a$:

$$L_o = 0.7 \cdot 2\mathbf{k} \cdot \alpha \cdot l_a = 1.4\mathbf{k} \cdot \alpha \cdot l_a. \tag{4}$$

Combining Eq. 3 and Eq. 4, we get the average in-degree per neuron

$$k_{in} = (L_c + L_o)/N = \alpha\, l_a (N - 0.4\mathbf{k})/N, \tag{5}$$

which, taking, without loss of generality, $l_a = 1$, gives us

$$\alpha = \frac{k_{in} N}{N - 0.4\mathbf{k}}. \tag{6}$$

The total number of edges in the network is given by $m = 4k_{in}N$ (note that, here, N denoted the number of neurons per module). Inserting the computed m, L_c, and α into Eq. 2 we get

$$Q = \sum_{c=1}^{4} \left(\frac{L_c}{4k_{in}N} - \left(\frac{k_{in}N}{4k_{in}N} \right)^2 \right) = 4 \left(\frac{(N - 1.8\mathbf{k})k_{in}N}{4(N - 0.4\mathbf{k})k_{in}N} - \frac{1}{16} \right) = \frac{N - 1.8\mathbf{k}}{N - 0.4\mathbf{k}} - \frac{1}{4}. \tag{7}$$

Interestingly, the final result does not depend on the choice of k_{in}—which gives us some degree of freedom to select a reasonable value for it in simulations (we took $k_{in} = 30$). The computed modularity closely matches the observations from network generation (minor discrepancies are expected due to variable degrees and actual numbers of synapses in every simulation. cf. Table S2).

		simulations, for different k_{in}			
	analytic	$k_{in} = 15$	20	25	30
k=0	0.750	0.748	0.749	0.749	0.749
k=1	0.715	0.706	0.706	0.705	0.705
k=3	0.642	0.621	0.619	0.618	0.616
k=5	0.566	0.535	0.533	0.532	0.530
k=10	0.361	0.322	0.322	0.322	0.324
k=20	−0.125	−0.102	−0.089	−0.074	−0.057
merged	0	0.018	0.018	0.019	0.019

Table S2. Modularity Q for different k vs. k_{in} combinations. Analytically, Q is independent from k_{in}, which is closely matched by the values measured in simulations.

C. Dynamics

To model neuronal behaviour, we use quadratic integrate-and-fire dynamics [80] with synaptic depression [86], which is implemented in a reduced form as in Ref. [18]. The neuron population consists of 20% inhibitory and 80% excitatory neurons, where inhibitory currents are modeled to have a higher amplitude and a slower decay time than excitatory ones [49, 87], cf. Table S3. Dynamic parameters of the model were chosen so that the network resembles regular spiking neurons [80] and the frequency of network-wide events was between 3 to 12 per minute, as observed in the experiments. Note that the parameter combination that was ultimately used is not unique and other combinations could yield the same burst frequency [88].

Independent of the neuron type, membrane dynamics are described through two coupled differential equations[2] for the membrane potential v and the recovery variable u:

$$\tau_v \, \dot{v} = a \, (v - v_{\mathrm{ref}}) \, (v - v_{\mathrm{thr}}) - u + I_{\mathrm{AMPA}} - I_{\mathrm{GABA}}, \tag{8}$$

$$\tau_u \, \dot{u} = b \, (v - v_{\mathrm{ref}}) - u, \tag{9}$$

$$\text{if } v \geq v_{\mathrm{peak}} : \begin{cases} v \to v_{\mathrm{reset}}, \\ u \to u + u_{\mathrm{incr}}. \end{cases} \tag{10}$$

The first term in Eq. (8) describes the basic behavior of the membrane potential. Below threshold, $v < v_{\mathrm{thr}}$, the membrane potential slowly decays to the resting value v_{ref} depending on the characteristic time constant τ_v and leak factor a. Once the threshold is exceeded by repeated stimulation, the membrane potential rises quickly until the peak potential v_{peak} is reached, a spike is triggered, and the potential is reset to v_{reset}. The membrane potential is decreased through the recovery variable u, which is driven by the activation of K^+ currents and the inactivation of Na^+ currents [80]. In practice, the coupling of Eqs. (8) and (9) determines the inter-spike interval and implements an effective refractory period.

The coupling of neurons is realized through excitatory and inhibitory current terms in Eq. 8: I_{AMPA} and I_{GABA} consist respectively of all excitatory and inhibitory currents arriving from the rest of the network. Each spike from a presynaptic neuron instantaneously increments the current term of the postsynaptic neuron. Note that in Ref. [18] small membrane fluctuations were implemented through an additional term, which we here omit to control the level of noisy input through a single control parameter.

Whenever an excitatory (inhibitory) pre-synaptic neuron spikes, it emits a current I that increments (decrements) the membrane potential of the post-synaptic neuron. The strength of the current depends on the amount of pre-synaptic resources (associated with the available neurotransmitters). To model the synaptic currents I and the level of synaptic resources ($R = 1$ for full available resources, $R = 0$ for full depletion), every neuron has three additional dynamic variables:

$$\tau_{\mathrm{AMPA}} \, \dot{I}_{\mathrm{AMPA}} = -I_{\mathrm{AMPA}}, \tag{11}$$

$$\tau_{\mathrm{GABA}} \, \dot{I}_{\mathrm{GABA}} = -I_{\mathrm{GABA}}, \tag{12}$$

$$\tau_R \, \dot{R} = 1 - R, \tag{13}$$

$$\text{if } v \geq v_{\mathrm{peak}} : R \to \beta \, R. \tag{14}$$

Note that I respectively describes all excitatory and inhibitory currents that arrive at the neuron, whereas R scales the outgoing current ($0 \leq \beta \leq 1$). Whenever a pre-synaptic neuron of type x spikes, the respective post-synaptic current term (AMPA or GABA) is incremented instantaneously:

$$I_{\mathrm{x,post}} \to I_{\mathrm{x,post}} + j_{\mathrm{x,pre}} \, R_{\mathrm{pre}} \, , \tag{15}$$

where $j_{\mathrm{x,pre}}$ is a constant to describe the current strength that depends on the type of the pre-synaptic neuron. From Eqs. (11)–(13), we see that I_{x} decay to 0 with a characteristic time τ_{x} and R slowly recovers to 1 with τ_R. In general, τ_R is much longer than the other time constants (see Table S3).

D. Stimulation

To incorporate optogenetic stimulation, the model features a controlled source of noise. The excitatory current arriving at each neuron is increased by small spikes of amplitude j_m generated randomly by a Poisson process

$$I_{\mathrm{AMPA}} \to I_{\mathrm{AMPA}} + j_m \quad \text{at rate} \quad h \, , \tag{16}$$

where h denotes the "synaptic noise rate" that serves as our control parameter when investigating the interplay of modularity and stimulation (main Figs. 3, 4 and Fig. S4).

In the main manuscript, we consider a baseline noise level to all neurons at $h = 80$ Hz, which accounts for miniature synaptic potentials ("minis") even in the absence of stimulation [18]. To mimic the experimental stimulation within two modules, additional Poisson noise at 20 Hz is applied to the neurons in those modules. Note that, because Poisson noise is additive, a local increase of the baseline input to 100 Hz would be equivalent.

---

[2] We express the equations in reduced form, and, for readability, omit the resistance R by denoting $I := RI^*$.

Parameter	Description	References
	Topology	[18]
$N = 160$	Number of neurons, out of which 20% inhibitory	[49, 87]
$200\,\mu m \times 200\,\mu m$	Substrate area per module (4 modules)	
$\rho = 1000\,mm^{-2}$	Density of plated neurons	
$r_s = 7.5\,\mu m$	Radius of somas (hard discs)	
$r_d \approx 150\,\mu m$	Radius of dendritic trees (soft discs), drawn from Normal dist. ($\mu = 150\,\mu m$, $\sigma = 20\,\mu m$)	
$l_a \approx 1000\,\mu m$	Length of axons, drawn from Rayleigh dist. ($\sigma = 800\,\mu m$)	
$\delta_a = 10\,\mu m$	Length of axon segments	
$\theta \approx 0^\circ$	Bending angle between segments, drawn from Normal dist. ($\mu = 0^\circ$, $\sigma = 57^\circ$)	
$\alpha \approx 0.3 - 2.7\,\%$	Probability to form a connection, per intersecting axon segment. Adjusted to realize k_{in}.	
$k_{in} \approx 30$	Average in-degree per neuron (all substrates)	[82]
	Dynamic variables	
v	Membrane potential	
u	Recovery variable	
I_{AMPA}	Excitatory current	
I_{GABA}	Inhibitory current	
R	Synaptic resources	
	Time scales	
$\tau_v = 50\,ms$	Time scale of the membrane potential v	
$\tau_u = 50\,ms$	Time scale of the recovery variable u	
$\tau_R = 20\,s$	Time scale of recovery of synaptic resources R	
$\tau_{AMPA} = 10\,ms$	Decay time of post-synaptic excitatory current	
$\tau_{GABA} = 20\,ms$	Decay time of post-synaptic inhibitory current	
	Dynamic constants	[18, 80]
$v_{ref} = -60\,mV$	Resting potential	
$v_{thr} = -45\,mV$	Threshold potential	
$v_{peak} = 35\,mV$	Peak potential, after v_{thr} is passed, rapid growth towards v_{peak}	
$v_{reset} = -50\,mV$	After-spike reset value of the membrane potential v	
$u_{incr} = 50\,mV$	After-spike increment value of recovery variable u	
$a = 0.5\,mV^{-1}$	Leak factor	
$b = 0.5$	Sensitivity of u to sub-threshold fluctuations of v	
$j_{AMPA} = 45\,mV$	AMPA current strength	
$j_{GABA} = 50\,mV$	GABA current strength	
$\beta = 0.8$	$R \to \beta R$ after spike, here synaptic depletion, thus $\beta < 1$	
$h = 80 - 115\,Hz$	Rate for Poisson noise (80 Hz baseline, $0 - 35\,Hz$ stimulation)	
$j_m = 15\,mV$	Strength of Poisson noise (stimulation), applied on I_{AMPA}	
	Simulation settings	[89]
$T = 30\,min$	Simulation time (after 5 min thermalisation)	
$\delta t = 0.05\,ms$	Time-step of numeric time integration (Euler)	
$\approx 30\,min$	Wall-clock runtime per simulation	
50	Number of repetitions	

Table S3. Overview of parameters and variables of the microscopic model.

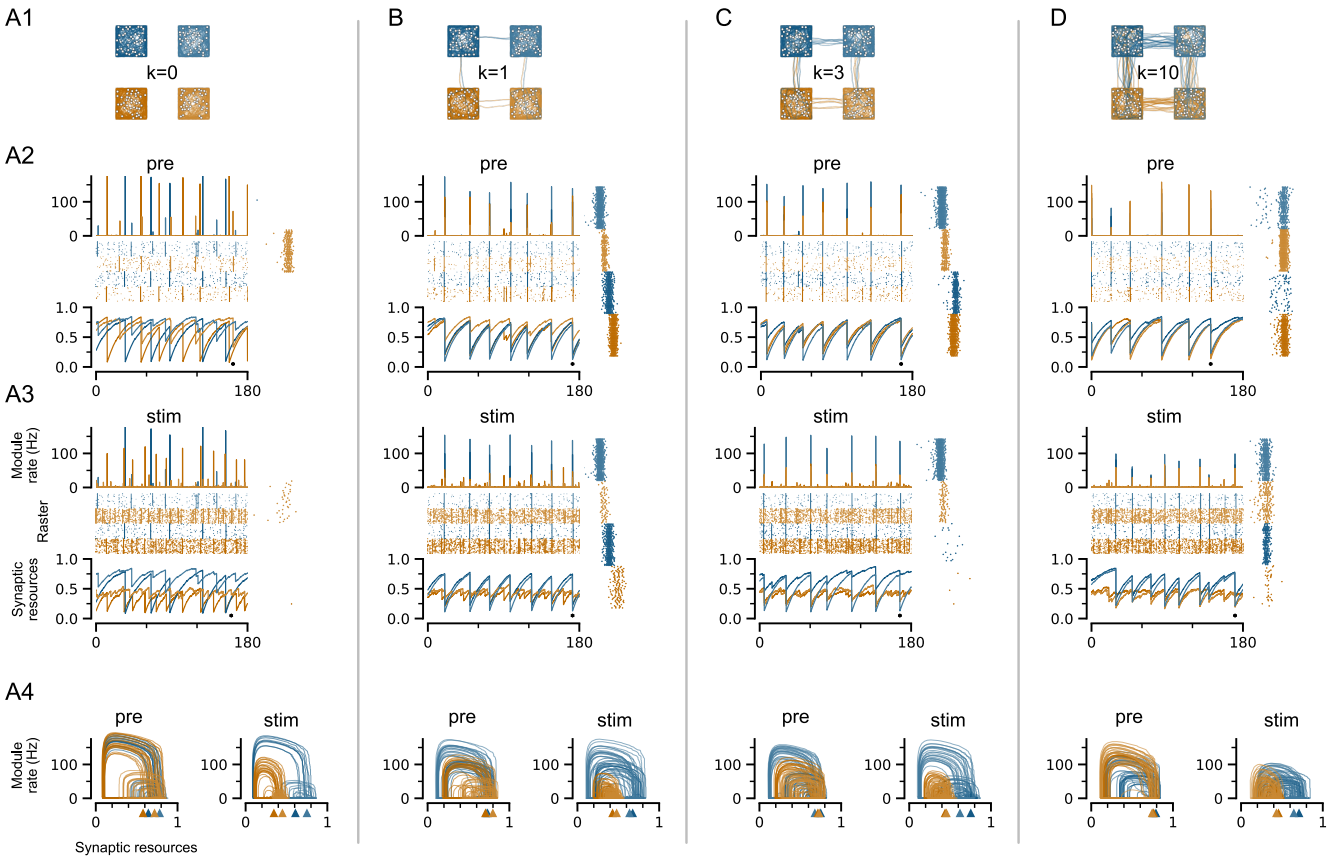

Figure S4. **Extended simulation details. A:** Overview of topology and dynamics for $k = 0$, corresponding to four independent modules. The dynamics plotted below (A2–A4) share this topology (and the RNG seed), and differ only in the stimulation rate. **A1:** Representation of the topology, featuring soma (white circles) and axons (colored lines). **A2, A3:** Module-level firing rate, raster plot and synaptic resources for a 180 s time window at 80 Hz baseline input (pre), and with an additional 20 Hz stimulation to the orange modules (stim). Synaptic resources are averaged across all neurons in a particular module and color-coded accordingly. The black dot denotes a 250 ms long zoom into the raster plot to illustrate a single event. **A4:** Charge-discharge cycles are illustrated in the resource-rate plane. Both synaptic resources and firing rates are calculated on the module level. 80 traces are shown (20 per module) where each trace lasts from end-time to end-time of two consecutive events (system-level bursting). The triangles on the x-axis indicate the average level of resources when an event starts. **B–D:** like A, but for $k = 1$, $k = 3$ and $k = 10$. **Summary:** In general, stimulation causes bursts to fire at lower rates (circle size) and to start at lower resource levels (triangles near x-axis). When modules are disconnected ($k = 0$), cycles reflect single-module properties independent of the stimulation. For intermediate connections ($k = 3$), the fluctuation in the trajectories of the non-targeted modules is strongest, but still retains module-dependent sizes. When intermodular connection is further increased ($k = 10$), cycles of non-targeted modules also decrease, as they activate together with targeted modules—while synchrony is maintained due to strong connections.

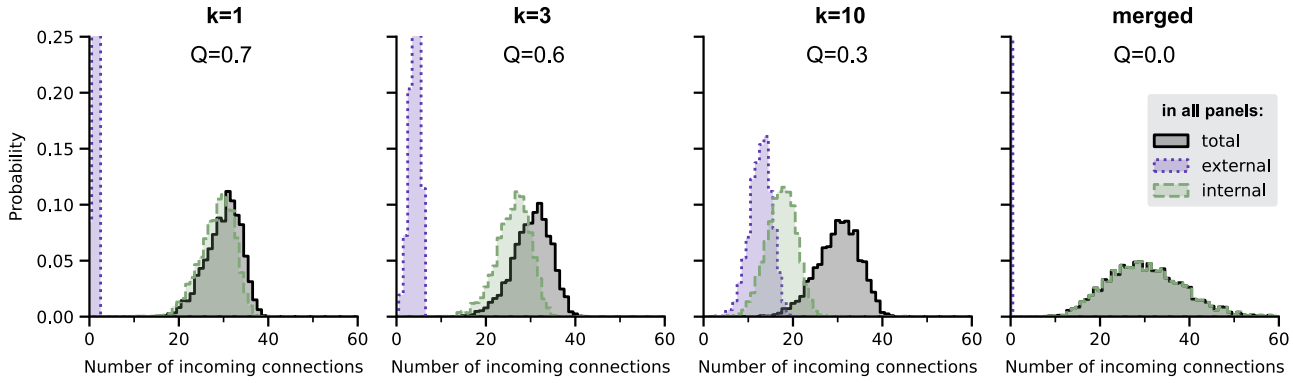

Figure S5. **In-degree distributions for different topologies.** For all topologies, the growth was adjusted to match an expected in-degree of $k_{\text{in}} \approx 30$. In simulations, modular cultures synchronize less strongly when average synaptic resources get depleted. This effect depends on the the number of incoming connections, which, determined by the topology, may greatly differ between *internal* connections (originating in the same module) and *external* connections spanning across modules. Distributions obtained from 20 independent realizations of each topology.

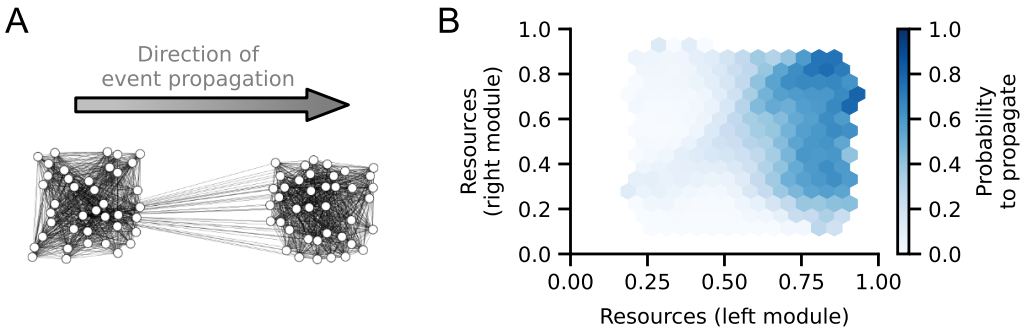

Figure S6. **Probability of event propagation.** We investigated the stochastic inter-modular connections, and in particular, how the probability of burst propagation depends on available resources. We performed simulations of two-module networks, where a single axon projected one-way from the left to the right module ($k = 1$, $\bar{k}_{\text{in}} = 30$). **A:** Sketch of the resulting connectivity. Causally, events can only propagate from the left to the right module. **B:** Probability that an event propagates from the source module (left) to the target module (right) as a function of the respective resource levels (module-average). To record events, 500 network realizations were sampled for a simulated duration of 5 min. Each simulation was repeated with different noise levels targeting the left, right or both modules. Noise frequency was varied from 0 to 35 Hz in steps of of 5 Hz. Events were mostly detected as for the main manuscript, but the system-wide rate threshold was fixed to 3 Hz to account for the altered topology. Events were classified as "successfully propagated" if both modules participated (module-level threshold crossing separated at most 100 ms). Coincidental events, where the right module fired alone, or by chance, just before the other module, were discarded. Thus, all considered events originate in the left module. For each of the remaining events, we extracted the average resources present in the source and target module, at the time of the event start. For all resulting (and binned) combinations of resources in the source- and target-module, we then calculated the propagation probability as the fraction of events that did indeed propagate. Note that we cannot set the combinations of resources directly (but, rather, we have to measure after adjusting them indirectly by setting the provided noise), which limits the accessible regions in the plotted phase plane. However, overall, the propagation probability is more sensitive to a depletion of resources in the originating module (x-axis) compared to depletion in the target module (y-axis).

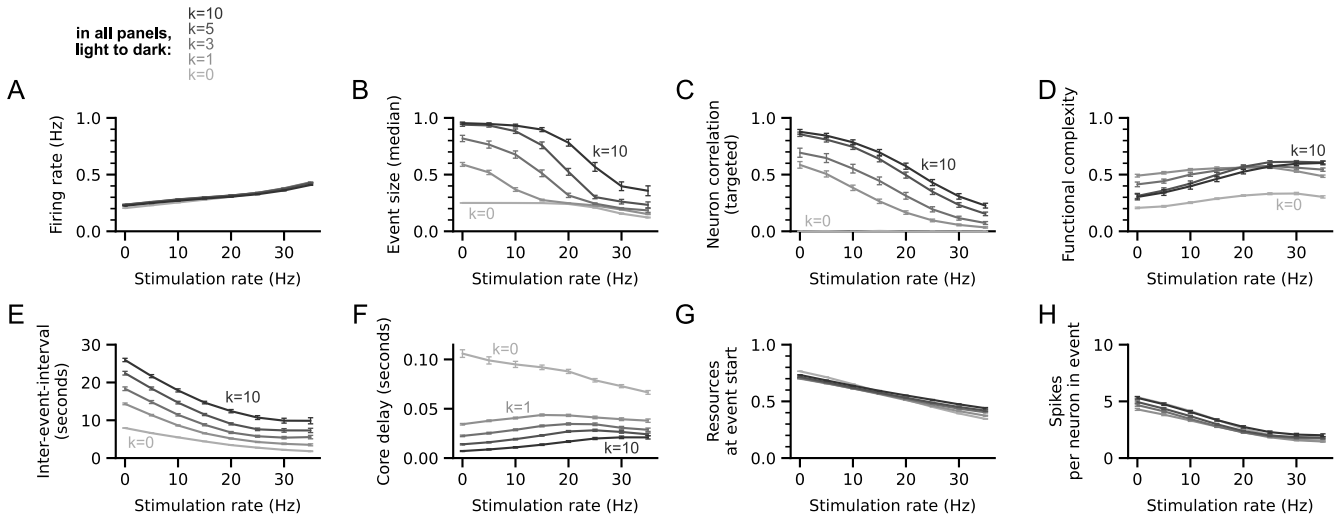

Figure S7. **In simulations, increasing noise decreases the intensity of network-wide events.** Dynamics depend on stimulation rate and the number of axons connecting modules, k. $k = 0$ is included as a control, indicating chance-level synchronization. **A:** Stimulation slightly increases the mean firing rate. **B:** Event size describes the fraction of neurons that fire at least one spike during a detected event (the chance-level event size that corresponds to one module is 0.25). Event sizes are larger for higher k but decrease under stimulation. **C:** Correlation of neuron pairs where both neurons are in modules targeted by stimulation (corresponding to main Fig. 4D, where the correlation of module-level firing rates is shown). **D:** Functional complexity is maximal at different stimulus intensity, depending on k. **E:** Inter-event-intervals decrease under stimulation. **F:** Core delays describe the the time between the respective highest-firing rate time-points when multiple modules contribute to an event. It serves as a proxy of the multi-module burst-duration. Note that $k = 0$ corresponds to chance-level. **G:** Consistent with the observed changes of charge-discharge cycles, the average module-level resources at the time point when an event starts decrease with increased stimulation rate. **H:** For every detected event we calculate the number of spikes each neuron contributed. Besides the decrease in the number of neurons that contribute (panel B), the decrease in spikes is a second mechanism to conserve (module-level) resources.

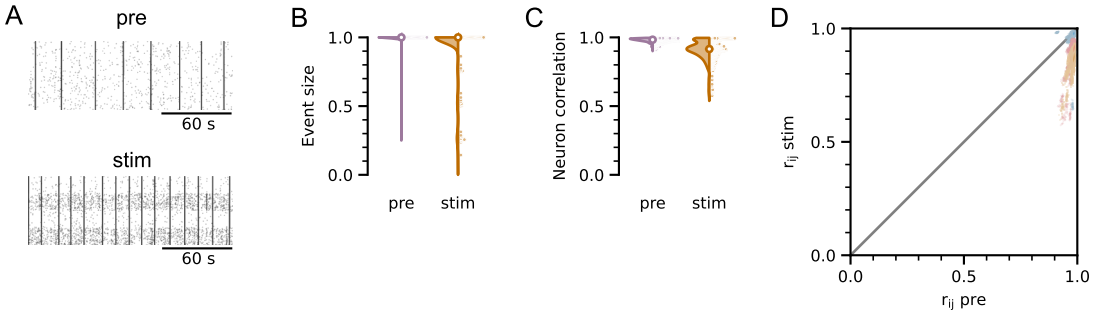

Figure S8. **Blocking inhibition in simulations weakens the desynchronizing effect of input**. Same as main Fig. 3, but with the current strength of inhibitory neurons set to $j_{\mathrm{GABA}} = 0$. Paremeters: $k = 3$, $k_{\mathrm{in}} \approx 30$.

E. Optical Recordings and Spike Detection

The raster plots from simulations that we presented in the main manuscript seem to differ from the experimental rasters, at first glance. In the following we explore that these differences are likely rooted in the sampling. Optical recordings are known to miss some spiking events, whereas simulations provide perfect sampling. In order to assess how these missing spikes affect the statistics of rates and bursting, we here considered a "virtual optical recording", in which some events are removed from simulated data, and then the statistics are compared.

Recently, Huang *et al.* [90] performed simultaneous patch-clamp recordings of spiking activity with fluorescence imaging, and computed the fraction of missing events. They found that isolated spikes are more likely to go undetected by fluorescence analyses, while consecutive spikes are detected more reliably. In order to mimic this phenomenology, we consider a probability $p_{\text{miss}}(n)$ of missing a single event when n spikes are presented in a time window of 250 ms, as reported in [90]. Then, the probability of missing m out of n spikes in a given time bin is given by a binomial distribution, $B(m, n, p_{\text{miss}}(n))$. The result of this process can be seen in Fig. S9. One can see that the raster gets "cleaner", since many of the asynchronous, isolated spikes are removed, thus giving a picture closer to that of the experiments. Notably, the burst-like events appear unaltered. We computed some core observables before and after applying the filter: the number of modules involved in events, the fraction of neurons involved (event size), inter-event-intervals, neuron correlations. Although detected firing rates decrease (not shown), and correlation distributions do not cover the low tail (corresponding to uncorrelated activity in-between events), the statistics of events and (median) correlations remain mostly the same. Thus, we conclude that results of simulations can be directly compared with those coming from the experiments, despite the fact that fluorescence misses some events. Since most missed events are isolated, bursting and synchronization statistics are not affected.

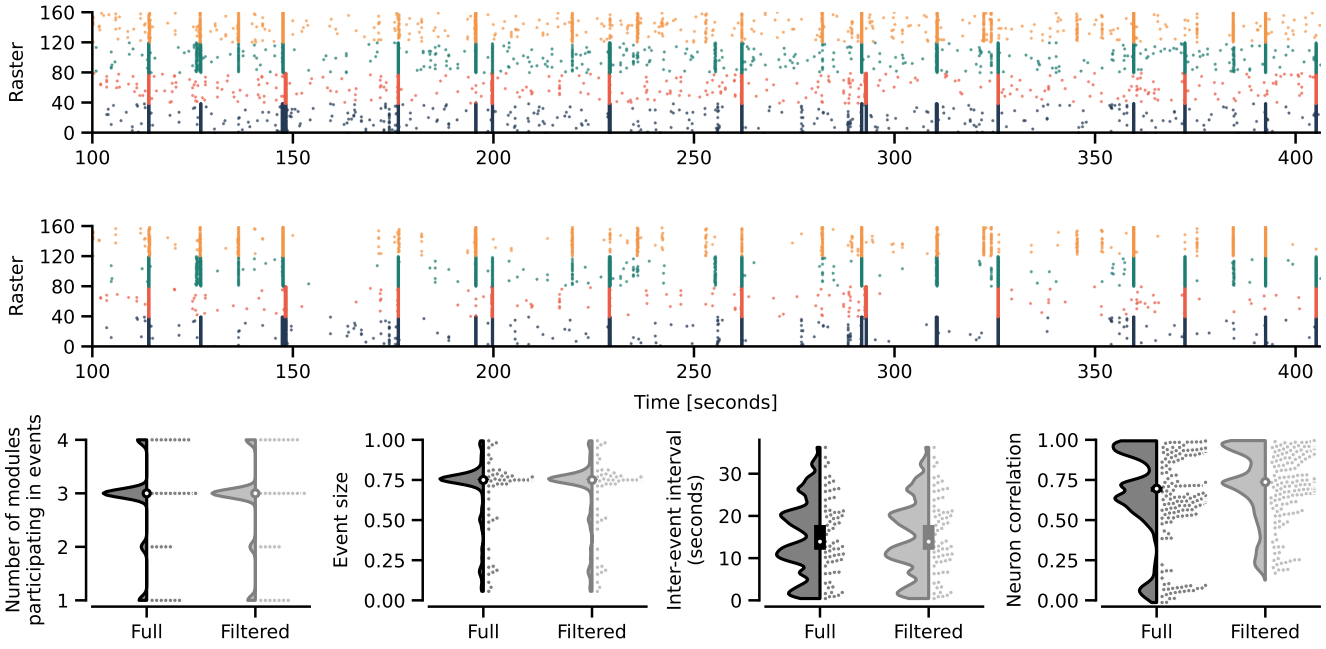

Figure S9. **Effect of missed spikes due to fluorescence in measured statistics.** Optical measurements predominantly miss isolated spikes from the recording. However, especially event-related observables are hardly affected. **A**: Original spike train at reference conditions ($k = 3$, pre). **B**: Filtered raster plot, after virtual optical recording. Note that we picked a realization that shows rather segregated activity, beyond the monotonic four-module synchrony. **C**: Observables employed in the main manuscript remain mostly unaffected when filtered. However, neuron-level correlations tend to be slightly higher when filtered. This is expected, as the missing of spikes occurs dominantly in the low-activity regime outside of synchronized events—which corresponds to uncorrelated firing of individual neurons.

3. DETAILS OF THE MESOSCOPIC MODEL WITH GATING MECHANISM

A. Mean-field Description of Module Dynamics

In order to link the mechanisms that we uncovered based on single-neuron dynamics and their impact on large-scale behavior, we developed a mesoscopic description that bridges local, finite-size aspects with conventional mean-field ideas to describe large populations of neurons through coarse-grained variables. In particular, the smallest spatial unit we consider in the following is a module. Each module i is characterized by only two stochastic variables: the module firing rate, $\rho_i(t)$, and the amount of available synaptic resources, $R_i(t)$. Notice that in a mean-field description individual neurons are assumed to be fully connected, meaning that the variables $\rho_i(t)$ and $R_i(t)$ do not present any dependence on space. The dynamics of an isolated module follows a rate model, which are a common choice to represent the activity of neuronal masses [75, 91–93]:

$$\dot{\rho}_i(t) = \underbrace{-\frac{1}{\tau_\rho}\rho_i(t)}_{\text{Decay}} + \underbrace{F\left[I_i(t)\right]}_{\text{Input}} + \underbrace{\sigma\,\xi_i\left(t\right)}_{\text{Noise}}, \tag{17a}$$

$$\dot{R}_i(t) = \underbrace{-\frac{1}{\tau_\mathrm{d}}\rho_i(t)\,R_i(t)}_{\text{Discharge}} + \underbrace{\frac{1}{\tau_\mathrm{c}}\left(R_0 - R_i(t)\right)}_{\text{Charge}}. \tag{17b}$$

Here, we also include short-term synaptic plasticity, Eq. (17b), to describe through one variable the average depletion and recovery of neurotransmitters of all neurons in the module, following Tsodyks and Markram [94, 95]. See Table S4 for a full description of all parameters.

At any given time t, module i receives a total input

$$I_i(t) = \underbrace{\rho_i(t)\,R_i(t)}_{\text{Self}} + \underbrace{h}_{\text{External}} + \underbrace{w\sum_{j\neq i} A_{ij}\,g_{ij}(t)\,\rho_j(t)\,R_j(t)}_{\text{Neighbours}}. \tag{18}$$

Input can stem from three sources: recurrent input from the module itself, external input accounting for, e.g., stimulation, and input from neighbouring modules (which depends on the state of the neighbour $\rho_j(t)R_j(t)$, the connections between modules $w\,A_{ij}$ and a novel gating variable $g_{ij}(t)$, see Section 3 C, below). The effect of inputs is implemented through a sigmoidal transfer function F, which maps the input to a change of the target-modules' rate:

$$F\left(I;\theta,a,b\right) = \begin{cases} b\frac{1-e^{-a(I-\theta)}}{1+e^{a\theta}e^{-a(I-\theta)}} & I > \theta\,, \\ 0 & I \leq \theta\,, \end{cases} \tag{19}$$

where θ, a, and b are constant parameters that determine the shape of the transfer function (Fig. S10A). The sigmoidal is selected such that $F\left(I=0;\theta,a,b\right)=0$, as is customarily done to ensure continuity of the function at zero input [91].

The dynamics of a single module are as follows: whenever the total input stays below the threshold $[I_i(t) < \theta]$, the transfer of inputs is suppressed, and the firing rate decays $[\rho_i(t) \to 0]$ with the (relatively short) time scale τ_ρ. During such times of low activity, synaptic resources are rarely used and slowly charge with time scale τ_c, until reaching the upper reference $[R_j(t) \to R_0]$. Notice that the amount of resources modulates the recurrent input [Eq. (18)], so that an isolated module without resources cannot increase its firing rate. On the other hand, once resources are charged and available, input from any source can trigger a feedback loop; a once-heightened firing rate causes the recurrent inputs to exceed the threshold, which again causes an increase in firing rate. Such self-accelerating episodes of high activity are commonly called bursts, and they will only terminate once the resources are depleted. For an isolated module, the noise term in Eq. (17a) ensures that such bursts occur from time to time, which reproduces well the behavior of in vitro systems (without enriched topologies), where large bursting events occur stochastically.

Here, depending on model parameters, an isolated module can also undergo stochastic burst cycles, where it alternates between states of high and low firing rates. Cycles tend to appear independently of parameters if the charging and discharging timescales are well separated and the maximum resources are enough to trigger the modules' feedback loop with a small fluctuation. The periods of cycles (and the burst duration) are determined by the timescales of resource charging (τ_c) and discharging (τ_d). This has been previously demonstrated in detail in Refs. [12, 96].

B. The Role of External Input

In the mesoscopic model, our experimental optogenetic stimulation is accounted for by the amplitude of module-level fluctuations σ, and the external input h in Eq. (18). In particular, this input is supplied to all modules at constant rate[3]; it is independent of the gate state, firing rate and resources. Consistent with the SNN-simulations, we find that an increase in external input decreases the amplitude of charge-discharge cycles in the resource-rate plane (Fig. S10C), and, if the gating mechanism is enabled, it helps to desynchronize modules (Fig. S11). This raises the question: how does external input decrease the amplitude of charge-discharge cycles?

Let us consider an isolated module at different values of h, without input from neighbours, and without fluctuations ($\sigma = 0$, Fig. S10B). For small h, no matter how we initialize the system, it will always end up in the charged state with zero firing rate and fully charged resources. For sufficiently large h, the system is in an input-driven regime that is characterized by high firing rates and low synaptic resources. The transition into this regime is discontinuous (Fig. S10B), and can be explained by the non-linear activation function (Eq. 19, Fig. S10A): only once all collected inputs exceed θ, does a rate change occur — and for the considered case of no neighbours, the only possible sources are h and the modules' recurrent input ($\rho_i R_i$). Once the system is in the input-driven regime, the total input always overcomes the decay, leading to the stationary dynamics with $\rho_i(t) > 0$. In neither of the above cases does the system undergo full (and repeated) charge-discharge cycles.

Parameter	Description
	Dynamic variables
$\rho_i(t)$	Firing rate (or activity) of module i
$R_i(t)$	Available synaptic resources in module i
$I_i(t)$	Total input arriving at module i
$\xi_i(t)$	Gaussian noise (mean 0, variance 1)
	Dynamic constants
$R_0 = 1$	Baseline synaptic resources
$\sigma = 0.1$	Intensity of (additive) background noise
$h = 0.0 - 0.3$	External input (rate), supplied to all modules
	Time scales
$\tau_\rho = 1$	Time scale of module rates (decay back to baseline)
$\tau_\mathrm{d} = 5$	Time scale of discharging synaptic resources
$\tau_\mathrm{c} = 40$	Time scale of charging synaptic resources
$\tau_\mathrm{gd} = 1$	Time scale of disconnecting gates
$\tau_\mathrm{gc} = 20$	Time scale of (re-)connecting gates
	Input transfer sigmoid
$\theta = 0.2$	Activation threshold, for input below θ no transfer
$a = 1.6$	Knee (abruptness of change) mapping module input to rate change
$b = 20.0$	Input gain of the function
	Gates and module coupling
$g_{ij}(t)$	Gate states. 1 if connected (transmitting activity), 0 else
Ω_{ij}	Rates at which gates connect/disconnect
A_{ij}	Adjacency matrix of modules. 1 if coupled/neighbouring, 0 else
$w = 0 - 0.15$	Coupling strength between modules
$a_\mathrm{g} = 10$	Knee of sigmoid mapping $R_j(t) \to \Omega_{ij}$
$\theta_\mathrm{g} = R_0/2$	Threshold of resources below which gates start to disconnect
	Simulation settings

Table S4. Overview of parameters and variables of the mesoscopic model.

[3] The constant rate in the mean-field picture is motivated microscopically by the Poisson spiking of every neuron in the population.

Next, let us next consider the isolated module, but with fluctuations ($\sigma \neq 0$, Fig. S10C). From Eq. (18), we note that h contributes as a linear term in the exponents $(I - \theta)$ of the transfer function Eq. (19). Thus, increasing h is equivalent to lowering the threshold θ, which determines how easily a burst can start due to fluctuations of a given amplitude σ. Thus, when the external input is increased $h \to \theta$, the module bursts more frequently and the average amount of available resources decreases. Due to the effectively lower threshold, even at the decreased resources, fluctuations can start a (less intense) burst. Together, this manifests in smaller charge-discharge cycles.

How do h and σ relate to the optogenetic stimulation in the experiments? As h describes the *average* external input to the underlying neuron population, the random optogenetic stimulation of individual neurons corresponds to an increased h. Consistently, increasing h causes higher activity in the mesoscopic model, as we also observed in experiments during stimulation. Because the targets of optogenetic stimulation are random, stimulation also corresponds to an increase of the module-level noise (an increase in σ). Reconsidering Fig. S10C, we see that increasing σ also decreases the size of charge-discharge cycles (as long as $h < \theta$). When fluctuations have a larger amplitude, they are more likely to push the module away from the stable point at high resources, triggering a burst. Thus, the average amount of resources at which bursts occur is lowered — just as in the case when increasing h. Thus, h and σ have a similar effect. In the following, we keep $\sigma = 0.1$ fixed and focus on systematically varying h.

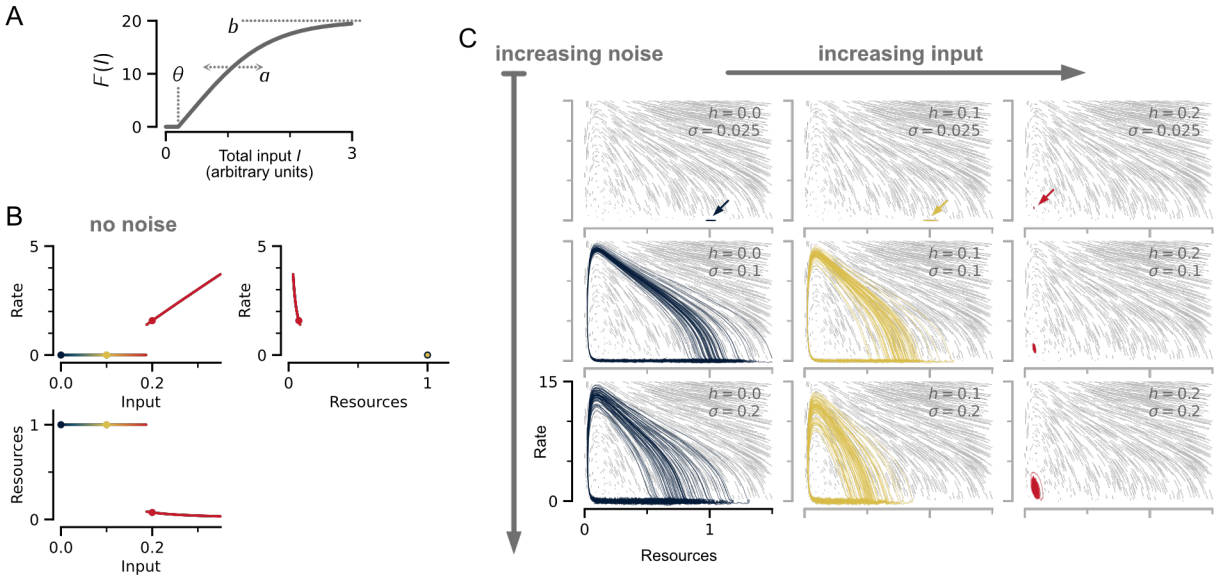

Figure S10. **Interplay of noise and external input for individual modules.** In the absence of fluctuations ("no noise", $\sigma = 0$), an isolated module will always end up at a stable fixed point. Charge-discharge cycles can only be triggered by sufficiently large fluctuations. **A:** Sketch of the transfer function $F(I; \theta, a, b)$ mapping the total input arriving at a module to a rate change. **B:** The position of the fixed point depends on the external input h. Colors scale from blue (low input) to red (high input) and match across panels to show how the fixed point moves in different representations. Bigger dots correspond to the values of h shown in panel C. As h is increased, the system undergoes a discontinuous transition to the input-driven (up) state, near $h \approx \theta = 0.2$, see accompanying text. **C:** Charge-discharge cycles in the Resource-Rate plane for simulations that include noise. Gray background lines indicate the deterministic flow field and derive from short, equally long time-integrations of Eqs. 17b and 17a (excluding the noise term and inputs from other modules). Long gray lines indicate fast dynamics and short lines indicate slow dynamics. The colored lines are example trajectories of the full model for a single module, including noise but without interacting neighbors. **C, top to bottom**: Increasing σ. Independent of external input h, only fluctuations can trigger a discharge by perturbing the module sufficiently far from the fixed point. **C, left to right**: Increasing h. For small $h \ll \theta = 0.2$, fluctuations trigger a fast discharge (bursting at high rates, depleting resources). Once resources are depleted, the module slowly recovers resources at rates near zero. For larger $h \geq \theta$, the system is in the input-driven regime of continuous firing at medium rates and low resources (right column). In this regime, fluctuations cannot start a burst (and the characteristic large cycles), because no resources are available.

C. Stochastic Gates as Connections between Mesoscopic Modules

In a mean-field formulation, one assumes that connectivity in the neuron population is all-to-all — an assumption which we here clearly violate when neurons are predominantly confined to grow connections within modules. As

we illustrate in the following, this manifests in the way modules synchronize and necessitates the introduction of a stochastic gating mechanism.

In the experimental cultures, modules connect because individual neurons grow an axon into a neighboring, coupled module. Thus, the total input projected from module j to i should depend on the average firing rate within the source module $\rho_j(t)$ and the number of connecting axons. Describing the average number of connecting axons through a continuous variable (the coupling strength w), and considering all coupled modules, then the total input to i would be $I_i(t) \sim w \sum_{j\neq i} A_{ij}\rho_j(t)$, where A_{ij} is the adjacency matrix describing links from j to i (1 if modules are coupled, 0 otherwise).

Clearly, in our experimental setup (and the simulations of LIF-neurons), the local topology plays a key role when coupling different modules, because only few individual neurons project to neighboring clusters ($1 \leq k \leq 10$). In particular, if $k = 1$ and the projecting neuron is already in a refractory state when a module-level burst occurs (or, by chance, it fails to release an action potential) then activity cannot spread between modules, preventing synchronization. Thus, the mean-field coupling strength (w) only partly captures the mechanism of the microscopic number of connecting axons (k): It accounts for the scaling of the input due to more connections but not for the increased probability of a successful transmission of activity. To account for this, we introduce a novel gating mechanism that incorporates the probabilistic nature of the connections between modules through a discrete gate variable. This allows us to maintain the advantages of the mean-field description (such as better analytic tractability) by accounting for the effects of low-level spatial structure while avoiding the necessity to explicitly incorporate it. As such, our model combines continuous and discrete variables and is an example of *hybrid stochastic systems*, which have also been employed to successfully describe single-cell dynamics [97].

A gate from module j to i is a discrete (Boolean) variable $g_{ij}(t)$ with two possible states: connected (1, activity can pass) or disconnected (0, activity cannot pass). Gates are not symmetric; g_{ij} can be connected while g_{ji} is disconnected, so that activity can spread in an inhomogeneous manner. Microscopically, disconnected gates represent a state in which the presynaptic neurons are exhausted. We have already included the state of the gates in the input to each module [Eq. (18)]. Input is projected from j to i only if both modules are coupled ($A_{ij} = 1$) and the gate is currently connected [$g_{ij}(t) = 1$]. The gates transition between states as follows: They (re-)connect at a constant rate, so that a disconnected gate recovers after a typical time τ_{gc}, and gates become more likely to disconnect as resources of the source-module are depleted. The stochastic transition-rates are:

$$\Omega_{ij}\,(0 \to 1) = \frac{1}{\tau_{\mathrm{gc}}}\,, \tag{20a}$$

$$\Omega_{ij}\,(1 \to 0) = \frac{1}{\tau_{\mathrm{gd}}}\left[1 - \frac{1}{1 + e^{-a_{\mathrm{g}}(R_j(t)-\theta_{\mathrm{g}})}}\right]\,, \tag{20b}$$

where a_{g}, and θ_{g} are parameters that control the (sigmoidal) response of the gate to the amount of available resources (cf. Fig. 4E in the main manuscript). For sufficiently small time steps δt, these rates directly correspond to the probability that a gate connects or disconnects, $P_{ij} \approx \Omega_{ij}\delta t$.

D. Gates Desynchronize Modules

How does the gating mechanism affect the interaction of multiple modules? Let us first consider how modules synchronize while gates are connected. In this case, the input from one module to another has the same effect that we saw for stochastic fluctuations and isolated modules. If a module is charged, a sufficiently strong perturbation can trigger a module-level burst. In addition, because bursts feature a high firing rate, they also cause severe input to all neighboring modules [Eq. (18)], which again acts as an initial perturbation, triggering subsequent bursts in those modules. Note that, because time scales are separated, the time of discharge during the burst is much quicker than the charging, so that all modules that participated in the system-level burst start recharging at what can be considered the "same time". Thus, they are also ready to burst again, and the system synchronizes. A crucial detail is that pairs of modules enter a recurrent feedback loop, just as we described for a single module; with constantly connected gates [$g_{ij} = 1$ in Eq. (18)], a change in ρ_j is very similar to a change of ρ_i. Of course, the recurrent feedback loop does not occur for vanishing coupling $w \to 0$, in which case modules become independent and could only synchronize by chance.

Our stochastic gating mechanism can disrupt the inter-module feedback loop for non-vanishing coupling: When a module starts bursting, its available resources are rapidly consumed, so that its outgoing gates will deactivate quickly ($\sim \tau_{\mathrm{gd}}$). Once a gate is disconnected, it will remain disconnected for a relatively long time ($\sim \tau_{\mathrm{gc}}$). In this period, if the module bursts again, activity cannot spread to the neighboring modules. Hence, if modules tend to burst with

a time scale faster than τ_{gc}, the recurrent feedback loop between modules is hindered, because the crucial initiating inputs cannot pass through the disconnected gates, and therefore the system cannot synchronize.

Finally, let us reconsider the external input h, an increase of which caused smaller charge-discharge cycles for isolated modules, by effectively lowering the threshold θ. Importantly, the smaller charge-discharge cycles correspond to more frequent bursts on the module level and lower average resources. For multiple modules connected by the gating mechanism, the lower resources cause the gates to be disconnected more often, and the fraction of bursts occurring in times of disconnected gates increases. Thus, it becomes less likely for a module-level burst to trigger a system-wide burst, because either gates are not ready or the target modules are not in the state of sufficiently charged resources.

To summarize, in order to desynchronize the modules of the mesoscopic model for non-vanishing coupling strengths, two ingredients are needed: i) a sufficiently strong amplitude of fluctuations to cause charge-discharge cycles, and ii) an inhomogeneous as well as stochastic coupling between modules, implemented through our novel gating mechanism. If both conditions are met, then the desynchronization can be facilitated by increasing the external input h to all modules (cf. Figs. S11 and S12).

4. CODE AVAILABILITY

Our source code for analysis and simulation is available via Github:
- Github: `https://github.com/Priesemann-Group/stimulating_modular_cultures`
- DOI: 10.5281/zenodo.7962283

Experimental data and processed analysis results are available via G-Node GIN:
- `https://gin.g-node.org/pspitzner/stimulating_modular_cultures`
- DOI: 10.12751/g-node.t77b3p

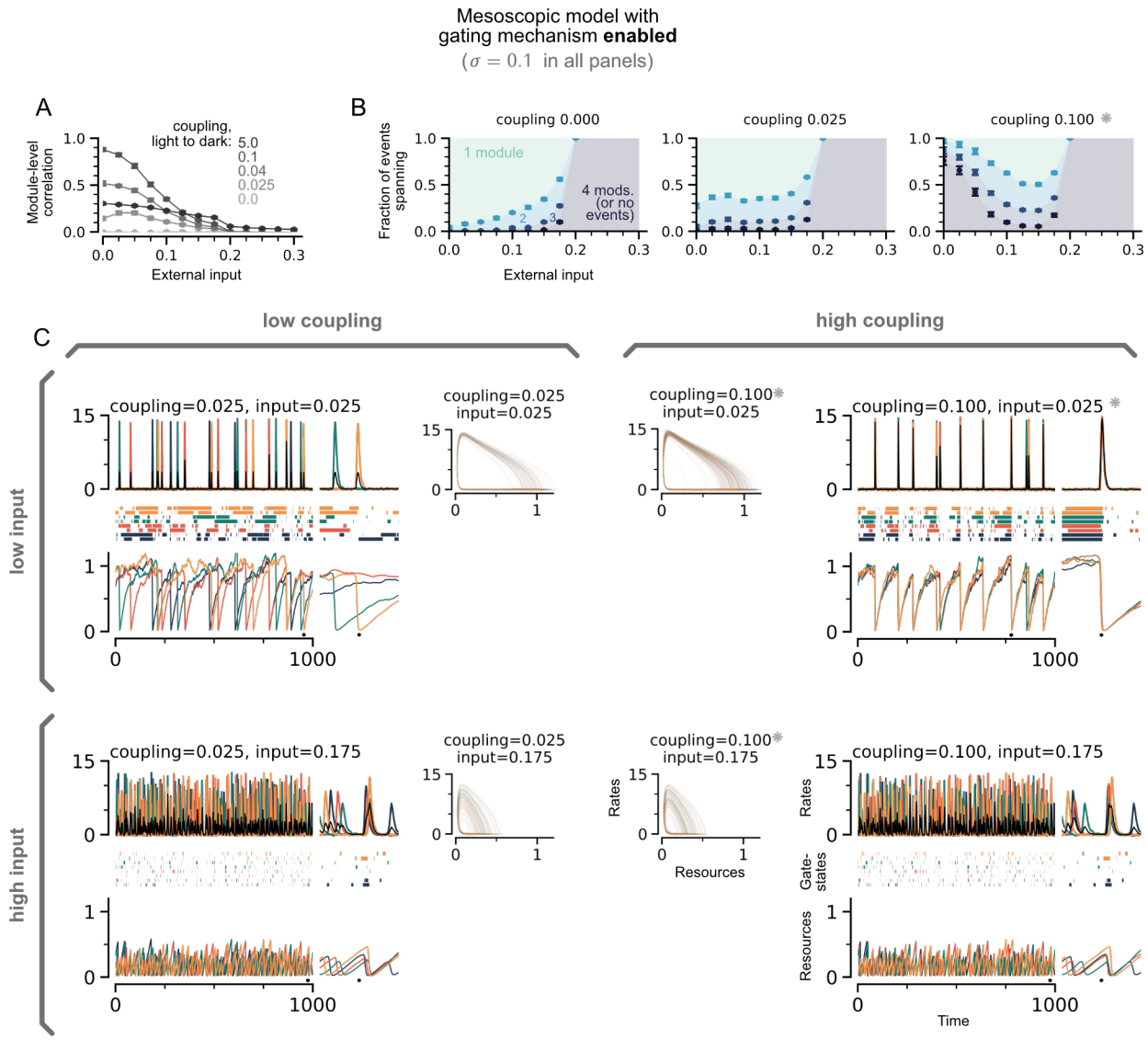

Figure S11. **Mesoscopic model with gating mechanism enabled, and varying stimulation to *all* modules.** With the gating mechanism, modules desynchronize when the coupling between modules is removed, or the external input is increased. Correlations between modules gradually decrease with increasing external input, until reaching the transition to the up state at $h \approx \theta = 0.2$. Note that very strong coupling (e.g. $w = 5.0$) leads to a saturation of the gating mechanism so that gates are always disconnected and modules can no longer synchronize, despite the strong coupling. Panels with a gray star are also presented in the main manuscript.

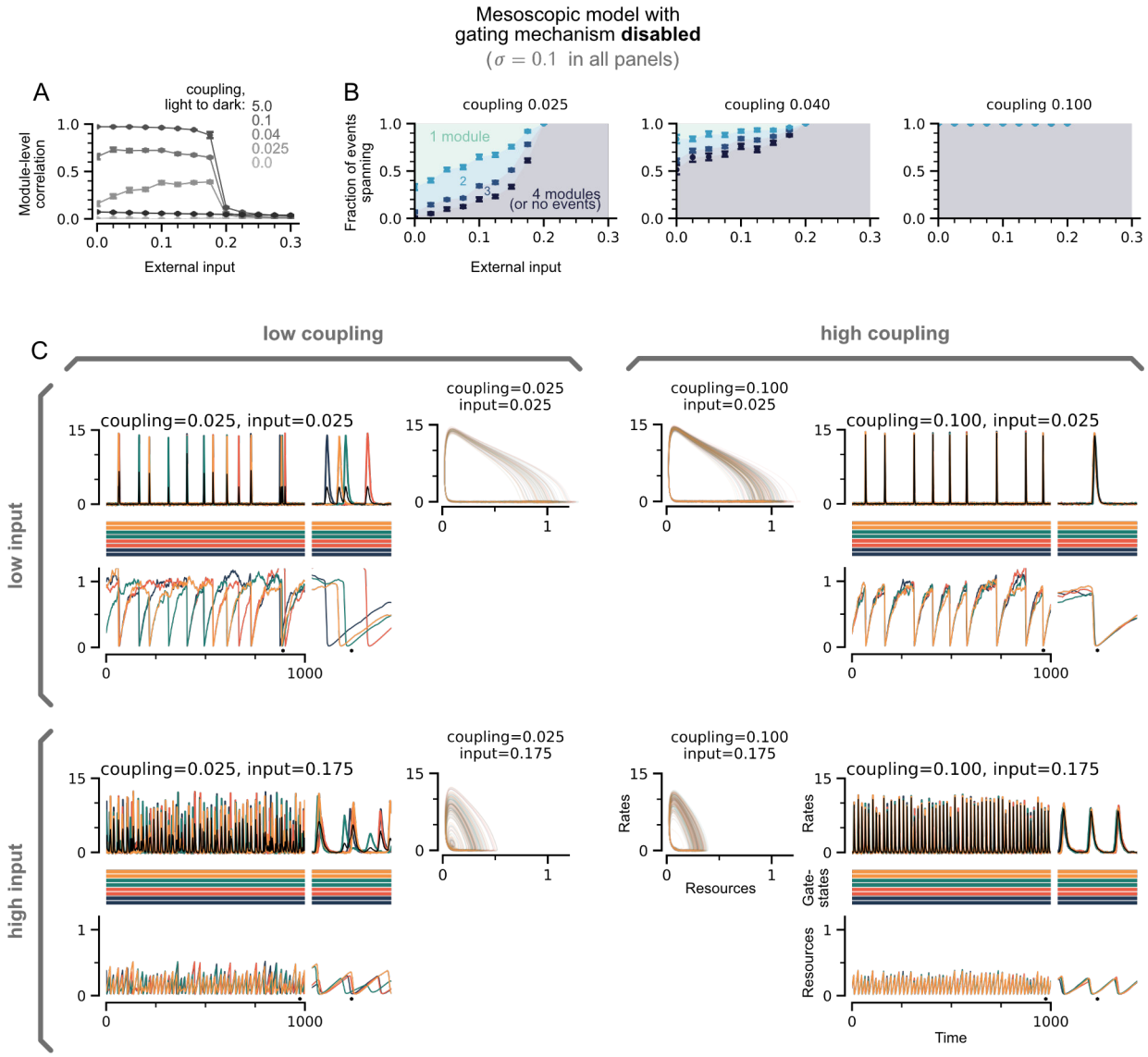

Figure S12. **Mesoscopic model with gates permanently connected, and varying stimulation to *all* modules.** Without the gating mechanism, modules only desynchronize for vanishing coupling. An increase of external input cannot desynchronize the modules. Correlations between modules drop abruptly as the system enters the input-driven up state $h \geq \theta = 0.2$.

5. DATA TABLES

Layout	**Condition**		targeted modules	across	non-targeted	all
single-bond	pre	median	0.72	0.76	0.81	0.76
		2.5	0.66	0.69	0.75	0.74
		97.5	0.81	0.82	0.85	0.82
	stim	median	0.22	0.31	0.73	0.41
		2.5	0.05	0.16	0.51	0.21
		97.5	0.31	0.41	0.74	0.44
	post	median	0.74	0.79	0.81	0.81
		2.5	0.56	0.61	0.80	0.73
		97.5	0.78	0.80	0.84	0.81
tripe-bond	pre	median	0.82	0.80	0.84	0.81
		2.5	0.80	0.68	0.78	0.78
		97.5	0.90	0.88	0.88	0.88
	stim	median	0.72	0.71	0.75	0.73
		2.5	0.27	0.31	0.71	0.46
		97.5	0.81	0.74	0.81	0.76
	post	median	0.81	0.84	0.86	0.85
		2.5	0.68	0.68	0.75	0.72
		97.5	0.90	0.89	0.89	0.89
merged	pre	median	0.92	0.89	0.91	0.91
		2.5	0.73	0.81	0.72	0.79
		97.5	0.95	0.92	0.93	0.92
	stim	median	0.59	0.51	0.74	0.62
		2.5	0.26	0.30	0.36	0.28
		97.5	0.84	0.85	0.89	0.87
	post	median	0.92	0.88	0.93	0.91
		2.5	0.87	0.83	0.82	0.85
		97.5	0.95	0.92	0.94	0.93
simulation (two modules targeted, $k = 3$)	pre (0.0 Hz)	median	0.83	0.81	0.82	0.82
		2.5	0.77	0.76	0.78	0.80
		97.5	0.86	0.84	0.85	0.84
	post (20.0 Hz)	median	0.33	0.50	0.80	0.58
		2.5	0.28	0.46	0.74	0.53
		97.5	0.44	0.53	0.84	0.63

Table S5. **Pairwise correlation sorted according to stimulation targets.** The data shown in the barplots (main Fig. 2D) compares neuron correlation and their dependence on the neuron's positions. For every neuron pair, both neurons could reside in the "targeted modules", both could reside in "non-targeted" modules, or "across", where one neuron is within a targeted module and the other one is not. The last column contains the ensemble of all pairs, irrespective of position. Note that for merged topologies, no modules exist but categorization is still possible, depending on whether a neuron is a potential stimulation target. The median corresponds the single-realization estimate (median neuron correlation), 2.5% and 97.5% are percentiles of the bootstrap distribution.

Layout	Condition	Percentile	Event size	Neuron correlation	IEI (seconds)	Core delays (ms)
single-bond	pre	50	1.00	0.77	18.97	39.17
		2.5	0.96	0.76	16.15	32.83
		97.5	1.00	0.78	21.35	45.26
	stim	50	0.46	0.40	6.23	70.00
		2.5	0.42	0.38	5.60	65.83
		97.5	0.50	0.42	6.92	77.83
	post	50	0.83	0.78	12.43	46.67
		2.5	0.81	0.77	11.43	42.24
		97.5	0.88	0.78	13.94	53.89
tripe-bond	pre	50	0.95	0.86	16.13	31.17
		2.5	0.95	0.86	12.96	27.91
		97.5	0.95	0.87	20.20	35.67
	stim	50	0.75	0.75	7.04	46.67
		2.5	0.73	0.74	6.33	39.92
		97.5	0.80	0.75	7.55	53.58
	post	50	0.95	0.88	17.13	34.83
		2.5	0.95	0.87	15.35	29.03
		97.5	0.95	0.88	19.69	41.25
merged	pre	50	1.00	0.89	19.85	35.83
		2.5	1.00	0.89	17.75	32.67
		97.5	1.00	0.90	23.67	40.42
	stim	50	0.75	0.72	5.35	37.67
		2.5	0.68	0.71	4.89	34.75
		97.5	0.79	0.75	5.87	40.00
	post	50	1.00	0.92	20.78	31.33
		2.5	1.00	0.91	15.73	28.17
		97.5	1.00	0.92	25.82	35.09
chemical	KCl =0 mM	50	0.81	0.72	42.40	59.25
		2.5	0.75	0.71	20.39	37.24
		97.5	0.88	0.74	48.64	100.00
	KCl =2 mM	50	0.94	0.76	20.01	104.50
		2.5	0.88	0.73	17.15	67.67
		97.5	0.94	0.78	22.34	153.33
bicuculline	0 µM	50	1.00	0.82	73.90	173.58
		2.5	0.85	0.80	56.74	129.58
		97.5	1.00	0.84	100.15	177.17
	20 µM	50	0.80	0.82	6.31	29.92
		2.5	0.80	0.80	4.97	26.87
		97.5	0.85	0.83	8.34	34.21
simulation (two modules targeted, $k = 3$)	pre (0.0 Hz)	50	0.81	0.84	18.76	18.00
		2.5	0.79	0.84	18.46	17.67
		97.5	0.81	0.85	19.06	18.17
	stim (20.0 Hz)	50	0.27	0.58	5.50	28.31
		2.5	0.26	0.57	5.38	27.75
		97.5	0.27	0.58	5.64	28.79

Table S6. **Statistics aggregated across trials.** For all the violins (main Figs. 2A,B and 3E) we plot aggregated observations (activity events, IEI or a pair of neurons contributing a correlation coefficient) that are collected across all trials. To get uncertainty estimates, we bootstrap the observations (a large number) and calculate the median for each of the 500 bootstrap samples. Then, considering all bootstrap samples, we get a distribution of where these medians fall. The percentiles of this distribution are plotted as the error sticks in the violins: the error bar from the 2.5% to the 97.5% and the white dot is located at the 50% (corresponding to the median of all bootstrap samples). Here, we use the median as we expect these distributions to be non-Gaussian, and skewed (for instance, the median event size of non-stimulated single-bond is 1, because the distribution is skewed — this would not be captured so well if we used the mean instead of the median).

Layout	Condition		Event size	Correlation coefficient	Functional complexity	IEI (seconds)	Core delays (ms)
single-bond ($N = 7$ realizations)	pre	mean	0.98	0.77	0.47	41.13	0.05
		sem	0.05	0.03	0.06	12.86	0.03
		max	1.00	0.85	0.75	109.98	0.24
		min	0.69	0.49	0.39	9.64	0.03
	stim	mean	0.52	0.39	0.68	9.45	0.07
		sem	0.11	0.06	0.07	2.91	0.02
		max	0.88	0.73	0.77	16.52	0.16
		min	0.25	0.21	0.47	4.41	0.04
	post	mean	0.93	0.79	0.47	18.57	0.05
		sem	0.05	0.04	0.04	8.14	0.02
		max	1.00	0.82	0.69	49.46	0.14
		min	0.75	0.47	0.38	9.60	0.02
triple-bond ($N = 7$ realizations)	pre	mean	0.96	0.82	0.39	34.41	0.05
		sem	0.04	0.04	0.06	9.76	0.01
		max	1.00	0.92	0.55	56.53	0.10
		min	0.75	0.72	0.24	7.06	0.02
	stim	mean	0.85	0.70	0.52	9.89	0.05
		sem	0.11	0.09	0.05	4.29	0.02
		max	1.00	0.90	0.67	41.80	0.11
		min	0.33	0.27	0.29	4.55	0.02
	post	mean	0.97	0.85	0.33	25.25	0.04
		sem	0.07	0.05	0.07	12.93	0.01
		max	1.00	0.91	0.55	47.84	0.06
		min	0.75	0.68	0.22	13.12	0.02
merged ($N = 7$ realizations)	pre	mean	0.99	0.90	0.30	61.41	0.05
		sem	0.02	0.05	0.07	24.62	0.03
		max	1.00	0.95	0.46	154.61	0.16
		min	0.94	0.69	0.16	3.14	0.02
	stim	mean	0.72	0.62	0.49	9.04	0.04
		sem	0.28	0.16	0.10	2.77	0.02
		max	1.00	0.94	0.70	16.11	0.14
		min	0.30	0.27	0.24	3.76	0.02
	post	mean	0.98	0.90	0.31	48.17	0.06
		sem	0.03	0.03	0.06	25.23	0.02
		max	1.00	0.93	0.48	158.83	0.09
		min	0.88	0.81	0.16	5.64	0.01
chemical ($N = 4$ realizations)	KCl =0 mM	mean	0.79	0.72	0.58	63.01	0.12
		sem	0.08	0.01	0.02	39.26	0.08
		max	1.00	0.75	0.62	177.93	0.34
		min	0.69	0.69	0.54	19.52	0.04
	KCl =2 mM	mean	0.92	0.75	0.48	34.50	0.15
		sem	0.05	0.09	0.09	12.55	0.09
		max	1.00	0.93	0.57	63.82	0.36
		min	0.78	0.53	0.21	17.38	0.03
bicuculline ($N = 5$ realizations)	0 µM	mean	0.90	0.76	0.49	90.78	0.15
		sem	0.16	0.05	0.06	13.84	0.03
		max	1.00	0.91	0.63	126.47	0.18
		min	0.25	0.65	0.38	55.56	0.07
	20 µM	mean	0.88	0.76	0.47	49.69	0.08
		sem	0.16	0.05	0.11	32.90	0.06
		max	1.00	0.94	0.65	134.48	0.30
		min	0.25	0.70	0.16	4.91	0.03

Table S7. **Trial-wise statistics.** For all the trial-level plots (main Fig. 1J and Figs. 2E–H) we consider observables of individual trials (realizations). Thus, the observable is calculated once for each realization (for example, functional complexity, the median neuron correlation in a trial, or the median event size in a trial). We then bootstrap these trials and get a distribution from the bootstrap samples. The white dot is the mean of the samples, the error bar indicates the mean plus/minus the bs-sample standard error and the extended thin line indicates that maximal/minimal value observed in any realization. Here, we use the mean because we expect these distributions to be normal.

REFERENCES AND NOTES

1. W. R. Softky, C. Koch, The highly irregular firing of cortical cells is inconsistent with temporal integration of random EPSPs. *J. Neurosci.* **13**, 334–350 (1993).

2. A. Arieli, A. Sterkin, A. Grinvald, A. D. Aertsen, Dynamics of ongoing activity: Explanation of the large variability in evoked cortical responses. *Science* **273**, 1868–1871 (1996).

3. M. E. Raichle, The restless brain. *Brain Connect.* **1**, 3–12 (2011).

4. J. Aru, J. Aru, V. Priesemann, M. Wibral, L. Lana, G. Pipa, W. Singer, R. Vicente, Untangling cross-frequency coupling in neuroscience. *Curr. Opin. Neurobiol.* **31**, 51–61 (2015).

5. A. Fornito, A. Zalesky, E. Bullmore, Fundamentals of brain network analysis. Academic Press (2016).

6. R. M. Hutchison, T. Womelsdorf, E. A. Allen, P. A. Bandettini, V. D. Calhoun, M. Corbetta, S. Penna, J. H. Duyn, G. H. Glover, J. Gonzalez-Castillo, D. A. Handwerker, S. Keilholz, V. Kiviniemi, D. A. Leopold, F. Pasquale, O. Sporns, M. Walter, C. Chang, Dynamic functional connectivity: Promise, issues, and interpretations. *Neuroimage* **80**, 360–378 (2013).

7. T. Matsui, T. Q. Pham, K. Jimura, J. Chikazoe, On co-activation pattern analysis and non-stationarity of resting brain activity. *Neuroimage* **249**, 118904 (2022).

8. J. M. Beggs, D. Plenz, Neuronal avalanches in neocortical circuits. *J. Neurosci.* **23**, 11167–11177 (2003).

9. R. Legenstein, W. Maass, Edge of chaos and prediction of computational performance for neural circuit models. *Neural Netw.* **20**, 323–334 (2007).

10. D. R. Chialvo, Emergent complex neural dynamics. *Nat. Phys.* **6**, 744–750 (2010).

11. L. Cocchi, L. L. Gollo, A. Zalesky, M. Breakspear, Criticality in the brain: A synthesis of neurobiology, models and cognition. *Prog. Neurobiol.* **158**, 132–152 (2017).

12. S. di Santo, P. Villegas, R. Burioni, M. A. Muñoz, Landau-Ginzburg theory of cortex dynamics: Scale-

free avalanches emerge at the edge of synchronization. *Proc. Natl. Acad. Sci. U.S.A.* **115**, E1356 (2018).

13. M. A. Muñoz, *Colloquium*: Criticality and dynamical scaling in living systems. *Rev. Mod. Phys.* **90**, 031001 (2018).

14. B. Cramer, D. Stöckel, M. Kreft, M. Wibral, J. Schemmel, K. Meier, V. Priesemann, Control of criticality and computation in spiking neuromorphic networks with plasticity. *Nat. Commun.* **11**, 2853 (2020).

15. D. Plenz, T. L. Ribeiro, S. R. Miller, P. A. Kells, A. Vakili, Self-organized criticality in the brain. *Front. Phys.* **9**, 639389 (2021).

16. N. Brunel, Dynamics of sparsely connected networks of excitatory and inhibitory spiking neurons. *J. Comput. Neurosci.* **8**, 183–208 (2000).

17. A. Renart, J. de la Rocha, P. Bartho, L. Hollender, N. Parga, A. Reyes, K. D. Harris, The asynchronous state in cortical circuits. *Science* **327**, 587–590 (2010).

18. J. G. Orlandi, J. Soriano, E. Alvarez-Lacalle, S. Teller, J. Casademunt, Noise focusing and the emergence of coherent activity in neuronal cultures. *Nat. Phys.* **9**, 582–590 (2013).

19. P. Fries, Rhythms for cognition: Communication through coherence. *Neuron* **88**, 220–235 (2015).

20. P. Villegas, P. Moretti, M. A. Muñoz, Frustrated hierarchical synchronization and emergent complexity in the human connectome network. *Sci. Rep.* **4**, 5990 (2014).

21. M. I. Rabinovich, P. Varona, A. Selverston, H. D. I. Abarbanel, Dynamical principles in neuroscience. *Rev. Mod. Phys.* **78**, 1213–1265 (2006).

22. E. Tognoli, J. A. S. Kelso, The metastable brain. *Neuron* **81**, 35–48 (2014).

23. O. Weinberger, P. Ashwin, From coupled networks of systems to networks of states in phase space. *Discrete Continuous Dyn. Syst. Ser. B* **23**, 2043–2063 (2018).

24. L. Donetti, P. I. Hurtado, M. A. Muñoz, Entangled networks, synchronization, and optimal network

topology. *Phys. Rev. Lett.* **95**, 188701 (2005).

25. A. Arenas, A. Diaz-Guilera, J. Kurths, Y. Moreno, C. Zhou, Synchronization in complex networks. *Phys. Rep.* **469**, 93–153 (2008).

26. Y. M. Lai, M. A. Porter, Noise-induced synchronization, desynchronization, and clustering in globally coupled nonidentical oscillators. *Phys. Rev. E* **88**, 012905 (2013).

27. M. Dazza, S. Métens, P. Monceau, S. Bottani, A novel methodology to describe neuronal networks activity reveals spatiotemporal recruitment dynamics of synchronous bursting states. *J. Comput. Neurosci.* **49**, 375–394 (2021).

28. A. Y. Y. Tan, Y. Chen, B. Scholl, E. Seidemann, N. J. Priebe, Sensory stimulation shifts visual cortex from synchronous to asynchronous states. *Nature* **509**, 226–229 (2014).

29. J. Zierenberg, J. Wilting, V. Priesemann, Homeostatic plasticity and external input shape neural network dynamics. *Phys. Rev. X* **8**, 031018 (2018).

30. R. M. Bruno, B. Sakmann, Cortex is driven by weak but synchronously active thalamocortical synapses. *Science* **312**, 1622–1627 (2006).

31. K. C.-K. Malina, B. Mohar, A. N. Rappaport, I. Lampl, Local and thalamic origins of correlated ongoing and sensory-evoked cortical activities. *Nat. Commun.* **7**, 12740 (2016).

32. H. Mizuno, K. Ikezoe, S. Nakazawa, T. Sato, K. Kitamura, T. Iwasato, Patchwork-type spontaneous activity in neonatal barrel cortex layer 4 transmitted via thalamocortical projections. *Cell Rep.* **22**, 123–135 (2018).

33. M. H. Friedberg, S. M. Lee, F. F. Ebner, Modulation of receptive field properties of thalamic somatosensory neurons by the depth of anesthesia. *J. Neurophysiol.* **81**, 2243–2252 (1999).

34. D. S. Greenberg, A. R. Houweling, J. D. Kerr, Population imaging of ongoing neuronal activity in the visual cortex of awake rats. *Nat. Neurosci.* **11**, 749–751 (2008).

35. W.-P. Chang, J.-S. Wu, C.-M. Lee, B. A. Vogt, B.-C. Shyu, Spatiotemporal organization and thalamic

modulation of seizures in the mouse medial thalamic-anterior cingulate slice. *Epilepsia* **52**, 2344–2355 (2011).

36. Ł. Kuśmierz, S. Ogawa, T. Toyoizumi, Edge of chaos and avalanches in neural networks with heavy-tailed synaptic weight distribution. *Phys. Rev. Lett.* **125**, 028101 (2020).

37. C. W. Lynn, D. S. Bassett, The physics of brain network structure, function and control. *Nat. Rev. Phys.* **1**, 318–332 (2019).

38. J. W. Scannell, M. P. Young, The connectional organization of neural systems in the cat cerebral cortex. *Curr. Biol.* **3**, 191–200 (1993).

39. J. W. Scannell, G. A. P. C. Burns, C. C. Hilgetag, M. A. O'Neil, M. P. Young, The connectional organization of the cortico-thalamic system of the cat. *Cereb. Cortex* **9**, 277–299 (1999).

40. C.-C. Hilgetag, G. A. P. C. Burns, M. A. O'Neill, J. W. Scannell, M. P. Young, Anatomical connectivity defines the organization of clusters of cortical areas in the macaque monkey and the cat. *Phil. Trans. R. Soc. Lond. B* **355**, 91–110 (2000).

41. D. Meunier, R. Lambiotte, E. T. Bullmore, Modular and hierarchically modular organization of brain networks. *Front. Neurosci.* **4**, 200 (2010).

42. M. P. van den Heuvel, E. T. Bullmore, O. Sporns, Comparative connectomics. *Trends Cogn. Sci.* **20**, 345–361 (2016).

43. W.-C. A. Lee, V. Bonin, M. Reed, B. J. Graham, G. Hood, K. Glattfelder, R. C. Reid, Anatomy and function of an excitatory network in the visual cortex. *Nature* **532**, 370–374 (2016).

44. H. Yamamoto, S. Moriya, K. Ide, T. Hayakawa, H. Akima, S. Sato, S. Kubota, T. Tanii, M. Niwano, S. Teller, J. Soriano, A. Hirano-Iwata, Impact of modular organization on dynamical richness in cortical networks. *Sci. Adv.* **4**, eaau4914 (2018).

45. J. L. Nathanson, Y. Yanagawa, K. Obata, E. M. Callaway, Preferential labeling of inhibitory and excitatory cortical neurons by endogenous tropism of adeno-associated virus and lentivirus vectors.

Neuroscience **161**, 441–450 (2009).

46. N. C. Klapoetke, Y. Murata, S. S. Kim, S. R. Pulver, A. Birdsey-Benson, Y. K. Cho, T. K. Morimoto, A. S. Chuong, E. J. Carpenter, Z. J. Tian, J. Wang, Y. L. Xie, Z. X. Yan, Y. Zhang, B. Y. Chow, B. Surek, M. Melkonian, V. Jayaraman, M. Constantine-Paton, G. K. S. Wong, E. S. Boyden, Independent optical excitation of distinct neural populations. *Nat. Methods* **11**, 338–346 (2014).

47. Y. Penn, M. Segal, E. Moses, Network synchronization in hippocampal neurons. *Proc. Natl. Acad. Sci. U.S.A.* **113**, 3341–3346 (2016).

48. G. Zamora-López, Y. Chen, G. Deco, M. L. Kringelbach, C. Zhou, Functional complexity emerging from anatomical constraints in the brain: The significance of network modularity and rich-clubs. *Sci. Rep.* **6**, 38424 (2016).

49. N. Sukenik, O. Vinogradov, E. Weinreb, M. Segal, A. Levina, E. Moses, Neuronal circuits overcome imbalance in excitation and inhibition by adjusting connection numbers. *Proc. Natl. Acad. Sci. U.S.A.* **118**, e2018459118 (2021).

50. S. Sadeh, C. Clopath, Inhibitory stabilization and cortical computation. *Nat. Rev. Neurosci.* **22**, 21–37 (2021).

51. D. Cohen, M. Segal, Network bursts in hippocampal microcultures are terminated by exhaustion of vesicle pools. *J. Neurophysiol.* **106**, 2314–2321 (2011).

52. E. Tibau, M. Valencia, J. Soriano, Identification of neuronal network properties from the spectral analysis of calcium imaging signals in neuronal cultures. *Front. Neural Circuits* **7**, 199 (2013).

53. E. A. Leicht, M. E. J. Newman, Community structure in directed networks. *Phys. Rev. Lett.* **100**, 118703 (2008).

54. S. Teller, C. Granell, M. De Domenico, J. Soriano, S. Gómez, A. Arenas, Emergence of assortative mixing between clusters of cultured neurons. *PLOS Comput. Biol.* **10**, e1003796 (2014).

55. M. A. Rabadan, E. D. De La Cruz, S. B. Rao, Y. Chen, C. Gong, G. Crabtree, B. Zu, S. Markx, J. A.

Gogos, R. Yuste, R. Tomer, An in vitro model of neuronal ensembles. *Nat. Commun.* **13**, 3340 (2022).

56. B. Pietras, V. Schmutz, T. Schwalger. Mesoscopic description of hippocampal replay and metastability in spiking neural networks with short-term plasticity, *PLOS Comput. Biol.* **18**, e1010809 (2022).

57. J. P. Neto, F. P. Spitzner, V. Priesemann, Sampling effects and measurement overlap can bias the inference of neuronal avalanches. *PLOS Comput. Biol.* **18**, e1010678 (2022).

58. E. Montbrió, D. Pazó, A. Roxin, Macroscopic description for networks of spiking neurons. *Phys. Rev. X* **5**, 021028 (2015).

59. Á. Byrne, R. D. O'Dea, M. Forrester, J. Ross, S. Coombes, Next-generation neural mass and field modeling. *J. Neurophysiol.* **123**, 726–742 (2020).

60. C. Bick, M. Goodfellow, C. R. Laing, E. A. Martens, Understanding the dynamics of biological and neural oscillator networks through exact mean-field reductions: A review. *J. Math. Neurosci.* **10**, 9 (2020).

61. I. V. Tyulkina, D. S. Goldobin, L. S. Klimenko, A. Pikovsky, Dynamics of noisy oscillator populations beyond the Ott-Antonsen ansatz. *Phys. Rev. Lett.* **120**, 264101 (2018).

62. S. M. Sherman, R. W. Guillery, The role of the thalamus in the flow of information to the cortex. *Phil. Trans. R. Soc. Lond. B* **357**, 1695–1708 (2002).

63. M. D. McDonnell and L. M. Ward, The benefits of noise in neural systems: Bridging theory and experiment. *Nat. Rev. Neurosci.* **12**, 415–425 (2011).

64. G. Shahaf and S. Marom, Learning in networks of cortical neurons. *J. Neurosci.* **21**, 8782–8788 (2001).

65. D. A. Wagenaar, R. Madhavan, J. Pine, S. M. Potter, Controlling bursting in cortical cultures with closed-loop multi-electrode stimulation. *J. Neurosci.* **25**, 680–688 (2005).

66. M. Chiappalone, P. Massobrio, S. Martinoia, Network plasticity in cortical assemblies. *Eur. J. Neurosci.* **28**, 221–237 (2008).

67. X. Zhang, F.-C. Yeh, H. Ju, Y. Jiang, G. F. W. Quan, A. M. J. VanDongen, Familiarity detection and memory consolidation in cortical assemblies. *eNeuro* **7**, ENEURO.0006–19.2020 (2020).

68. Y. Inglebert, J. Aljadeff, N. Brunel, D. Debanne, Synaptic plasticity rules with physiological calcium levels. *Proc. Natl. Acad. Sci. U.S.A.* **117**, 33639–33648 (2020).

69. S. Okujeni, U. Egert, Self-organization of modular network architecture by activity-dependent neuronal migration and outgrowth. *eLife* **8**, e47996 (2019).

70. S. Okujeni, U. Egert, Structural modularity tunes mesoscale criticality in biological neuronal networks. *J. Neurosci.* **43**, 2515–2526 (2023).

71. F. M. Krienen, M. Goldman, Q. Zhang, R. C. H. del Rosario, M. Florio, R. Machold, A. Saunders, K. Levandowski, H. Zaniewski, B. Schuman, C. Wu, A. Lutservitz, C. D. Mullally, N. Reed, E. Bien, L. Bortolin, M. Fernandez-Otero, J. D. Lin, A. Wysoker, J. Nemesh, D. Kulp, M. Burns, V. Tkachev, R. Smith, C. A. Walsh, J. Dimidschstein, B. Rudy, L. S. Kean, S. Berretta, G. Fishell, G. Feng, S. A. McCarroll, Innovations present in the primate interneuron repertoire. *Nature* **586**, 262–269 (2020).

72. S. Loomba, J. Straehle, V. Gangadharan, N. Heike, A. Khalifa, A. Motta, N. Ju, M. Sievers, J. Gempt, H. S. Meyer, M. Helmstaedter, Connectomic comparison of mouse and human cortex. *Science* **377**, eabo0924 (2022).

73. G. Tononi, O. Sporns, G. M. Edelman, A measure for brain complexity: Relating functional segregation and integration in the nervous system. *Proc. Natl. Acad. Sci. U.S.A.* **91**, 5033–5037 (1994).

74. L.-D. Lord, A. B. Stevner, G. Deco, M. L. Kringelbach, Understanding principles of integration and segregation using whole-brain computational connectomics: Implications for neuropsychiatric disorders. *Philos. Trans. A Math. Phys. Eng. Sci.* **375**, 20160283 (2017).

75. G. Deco, V. K. Jirsa, P. A. Robinson, M. Breakspear, K. Friston, The dynamic brain: From spiking neurons to neural masses and cortical fields. *PLOS Comput. Biol.* **4**, e1000092 (2008).

76. Y. Xu, M. Takai, T. Konno, K. Ishihara, Microfluidic flow control on charged phospholipidpolymer interface. *Lab Chip* **7**, 199–206 (2007).

77. H. Yamamoto, S. Kubota, Y. Chida, M. Morita, S. Moriya, H. Akima, S. Sato, A. Hirano-Iwata, T. Tanii, M. Niwano, Size-dependent regulation of synchronized activity in living neuronal networks. *Phys. Rev. E* **94**, 012407 (2016).

78. C. M. Hales, J. D. Rolston, S. M. Potter, How to culture, record and stimulate neuronal networks on micro-electrode arrays (MEAs). *J. Vis. Exp.* **39**, 2056 (2010).

79. T. Deneux, A. Kaszas, G. Szalay, G. Katona, T. Lakner, A. Grinvald, B. Rózsa, I. Vanzetta, Accurate spike estimation from noisy calcium signals for ultrafast three-dimensional imaging of large neuronal populations in vivo. *Nat. Commun.* **7**, 12190 (2016).

80. E. M. Izhikevich, Simple model of spiking neurons. *IEEE Trans. Neural Netw.* **14**, 1569–1572 (2003).

81. S. Sahara, Y. Yanagawa, D. D. M. O'Leary, C. F. Stevens, The fraction of cortical GABAergic neurons is constant from near the start of cortical neurogenesis to adulthood. *J. Neurosci.* **32**, 4755–4761 (2012).

82. J. Soriano, M. R. Martínez, T. Tlusty, E. Moses, Development of input connections in neural cultures. *Proc. Natl. Acad. Sci. U.S.A.* **105**, 13758–13763 (2008).

83. T. Takemuro, H. Yamamoto, S. Sato, A. Hirano-Iwata, Polydimethylsiloxane microfluidic films for in vitro engineering of small-scale neuronal networks. *Jpn. J. Appl. Phys.* **59**, 117001 (2020).

84. M. Newman, in *Networks* (Oxford University Press, ed. 2, 2018).

85. R. Guimerà, M. Sales-Pardo, and L. A. Nunes Amaral, Modularity from fluctuations in random graphs and complex networks. *Phys. Rev. E* **70**, 025101(R) (2004).

86. E. Alvarez-Lacalle and E. Moses, Slow and fast pulses in 1-D cultures of excitatory neurons. *J. Comput. Neurosci.* **26**, 475–493 (2009).

87. J. S. Isaacson, M. Scanziani, How inhibition shapes cortical activity. *Neuron* **72**, 231–243 (2011).

88. K. A. Ferguson, F. Njap, W. Nicola, F. K. Skinner, S. A. Campbell, Examining the limits of cellular adaptation bursting mechanisms in biologically-based excitatory networks of the hippocampus. *J. Comput. Neurosci.* **39**, 289–309 (2015).

89. M. Stimberg, R. Brette, D. F. Goodman, Brian 2, an intuitive and efficient neural simulator. *eLife* **8**, e47314 (2019).

90. L. Huang, P. Ledochowitsch, U. Knoblich, J. Lecoq, G. J. Murphy, R. C. Reid, S. E. J. de Vries, C. Koch, H. Zeng, M. A. Buice, J. Waters, L. Li, Relationship between simultaneously recorded spiking activity and fluorescence signal in GCaMP6 transgenic mice. *eLife* **10**, e51675 (2021).

91. H. R. Wilson, J. D. Cowan, Excitatory and inhibitory interactions in localized populations of model neurons. *Biophys. J.* **12**, 1–24 (1972).

92.M. Jedynak, Collective excitability in a mesoscopic neuronal model of epileptic activity. *Phys. Rev. E* **97**, 012204 (2018).

93. W. Gerstner, W. M. Kistler, R. Naud, L. Paninski, in *Neuronal dynamics: From single neurons to networks and models of cognition* (Cambridge Univ. Press, 2014).

94. M. V. Tsodyks, H. Markram, The neural code between neocortical pyramidal neurons depends on neurotransmitter release probability. *Proc. Natl. Acad. Sci. U.S.A.* **94**, 719–723 (1997).

95. D. Holcman, M. Tsodyks, The emergence of Up and Down states in cortical networks. *PLOS Comput. Biol.* **2**, e23 (2006).

96. V. Buendía, P. Villegas, R. Burioni, M. A. Muñoz, Hybrid-type synchronization transitions: Where incipient oscillations, scale-free avalanches, and bistability live together. *Phys. Rev. Research* **3**, 023224 (2021).

97.P. C. Bressloff, J. N. Maclaurin, Stochastic hybrid systems in cellular neuroscience. *J. Math. Neurosci.* **8**, 12 (2018).